Performance Characteristics of Coupled Laser Resonators

A DISSERTATION
SUBMITTED TO THE FACULTY OF THE GRADUATE SCHOOL
OF THE UNIVERSITY OF MINNESOTA
BY

Chenhao Wan

IN PARTIAL FULFILLMENT OF THE REQUIREMENTS
FOR THE DEGREE OF
DOCTOR OF PHILOSOPHY

James R. Leger

August, 2012

Acknowledgements

I would like to thank Professor James Leger for his inspiring guidance and continuous support during my PhD study. His invaluable mentorship not only teaches me the knowledge in optics but also leads me to learn how to independently analyze and solve research problems. It's been my great honor to be one of his PhD students.

My gratitude also extends to the professors who served on my preliminary and final oral exam committee, Anand Gopinath, Taner Akkin, and Joey Talgader for their advice on my research projects.

I am very grateful to previous and current research group members: Mercedeh Khajavikhan, Brad Tiffany, Ying Wan, Jordan Burch, Hung-Sheng Chiang, Di Lin, Greg Ingersoll and Shi Sha. I enjoyed spending time discussing questions and doing research with them.

My experiments were accomplished with great support from the machine shop. The custom mechanical parts made by Mark Fisher, Kevin Roberts and Dave Hultman were crucial to my projects.

It's been a joyful six year experience in Minnesota to get acquainted with many friends at the Hospitality Center for Chinese: Phyllis, Bud, Jennifer, Peter, Amy, Nate and Jerry.

Finally, I would like to thank my parents Yufa Wan and Meili Zhou. Their love and support is the source of every bit of my progress. It is my privilege to have the happiness and love brought by my wife Yue Tang. I would also like to say thank you to her parents Zhaonian Huang and Xiaomin Tang for their encouragement and support.

Dedication

This dissertation is dedicated to my parents and douzi.

Abstract

Conventional laser architectures are ultimately limited in maximum achievable power by one or more physical constraints. Both spectral beam combining and coherent beam combining provide alternative solutions to increase total system radiance. In particular, coherent beam combining promises to increase radiance while maintaining all the spectral and polarization features of an individual laser beam. One of the challenging aspects of coherent beam combining is to maintain the proper phase relationship between all the elements in the array. In the thesis, the sensitivity to path length changes is theoretically analyzed and experimentally explored in coherent combining architectures based on Fourier-plane spatial filtering. The supermodes of a two-laser spatially filtered cavity exhibit two distinctly different types of behavior depending on the path length error. When the error is small, the two modes present different cavity loss values and can be differentiated by gain. However, cavities containing path length errors greater than a critical value produce modes with identical losses and different resonant frequencies. The supermodes of tiled-aperture coherent beam combining cavities contain many lobes in the far field. Beam shaping techniques based on phase modifications convert the supermodes into desired shapes. The supermode of a self-Fourier cavity containing 21 lasers is converted to a quasi-flat-top shape and most power is delivered to the central lobe in the far field.

Table of Contents

List of Tables

List of Figures

Chapter1 Introduction

The history of lasers starts in the early 1960s when the first ruby laser was demonstrated at Hughes Research Laboratories [1]. Since then, efforts to obtain high-radiance laser sources have never stopped. High-radiance lasers are desirable for a number of applications, such as material processing, remote sensing and medical surgery. Conventional laser systems are limited in maximum achievable power by several physical effects. These effects include thermally induced aberrations, optical damage, optical Kerr nonlinearities and lasing in multiple spatial modes. For example, the heat generated in a crystal gain is not uniformly distributed and the effective index of refraction change causes the thermal lensing problem [2]. Another example is the output power limitation imposed by stimulated Brillouin scattering (SBS) thresholds in fiber lasers [3] [4]. For SBS, a high intensity source can create an acoustic wave in the fiber and the acoustic wave will then create refractive index variations within the fiber which in-turn scatter the pump light through Bragg diffraction. As the incident pump power is increased it will reach a maximum threshold in which no additional output power will be realized due to complete conversion to the backward scattered wave.

Beam combining techniques provide a way to realize high output power by using a number of lower-power and spatially separated gain elements. These techniques reduce the power per gain element while maintaining high total power and good beam quality.

There are two main categories of beam combining techniques: spectral beam combining and coherent beam combining.

Spectral beam combining techniques do not require the mutual coherence of multiple gain elements. They utilize laser emitters with non-overlapping optical spectra. The output spectrum of a spectral beam combining system becomes wider as the number of laser emitters becomes larger.

Coherent beam combining techniques work with mutually coherent beams and all of the gain elements operate with the same spectrum. The relative phases of the gain elements are accurately controlled such that the beams add constructively.

This dissertation presents a detailed theoretical analysis on path length sensitivity in the coherent beam combining architecture based on the Fourier plane spatial filtering. Modal properties of a two-gain-element cavity are thoroughly discussed. Analytical models and computer simulations are used to derive the eigenvalue equations that describe the beam propagation inside the cavity. A diode-pumped solid state laser cavity is designed and built for experimental verification of the path length sensitivity theory. The apparatus is designed based on polarization multiplexing to ensure the path length balance of the two beam channels. The experimental data demonstrate the two regions predicted by the theory: in small phase error region, the two modes have differential losses and only one mode can lase whereas in large phase error region, the two modes have the same loss and

both modes can lase simultaneously. Understanding the relationship of modal properties and phase errors is important to build efficient coherent beam combining resonators.

The supermodes of most coherently combined cavities contain multiple lobes in the far field. Laser beam shaping, the control of the irradiance and phase profile of the output of a laser, is an enabling technology to convert the supermodes to desired shapes. In this thesis, a design is shown to convert the fundamental supermode of a self-Fourier cavity containing 21 lasers into to a quasi-flat-top shape. 94.4% of the power is delivered to the central lobe in the far field.

Chapter 2 Spectral Beam Combining

Spectral beam combining (also called wavelength beam combining) is an incoherent beam combining technique that does not require mutual coherence. It uses an array of laser emitters with non-overlapping optical spectra. The beams are combined with a wavelength-sensitive optical element such as a diffraction grating. Spectral beam combing increases the output power at the expense of spectral broadening. Spectral beam combining is useful for applications that are concerned with power and is unsuitable for applications that require a narrow-bandwidth laser source.

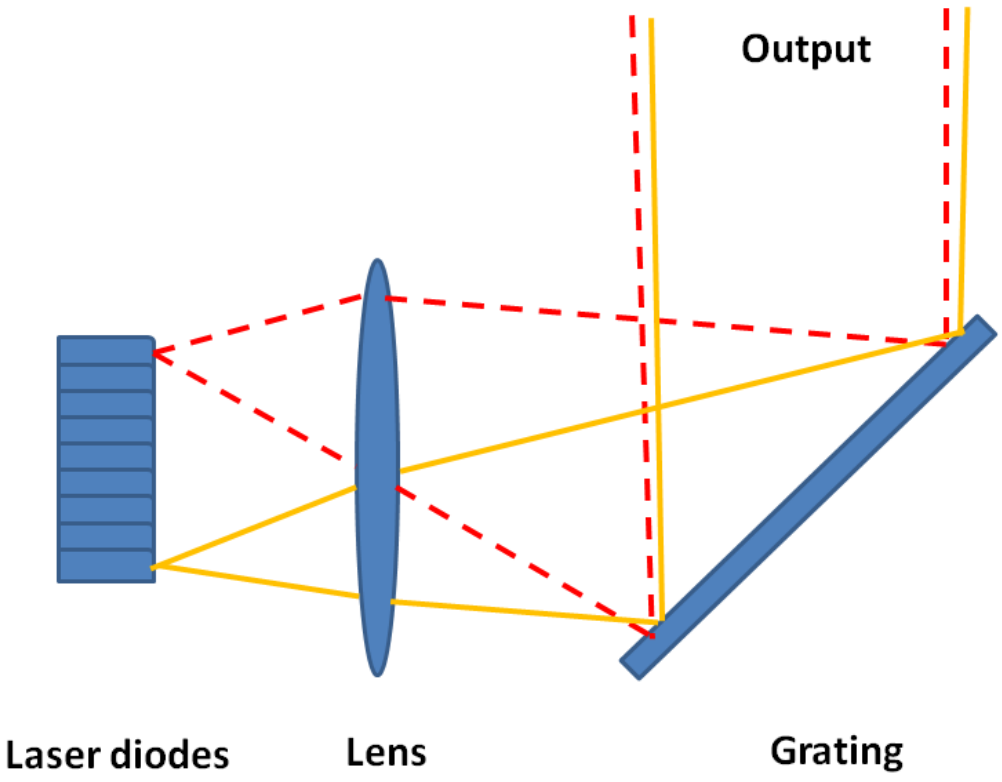

Fig. 2.1 Spectral beam combining of diode lasers

The configuration of the basic setup for spectral beam combining is shown in Fig. 2.1. An array of laser emitters of different wavelengths is positioned in parallel. The position of an array element is transformed to an angle of incidence on the diffraction grating by a lens. Coaxial propagation of the individual beams is realized by placing the diffraction grating one focal length away from the lens. Near-diffraction-limited diode laser arrays containing 100 elements by spectral beam combining have been demonstrated at MIT Lincoln Laboratory [5].

Spectral beam combining uses an array of laser emitters with non-overlapping optical spectra. If there is an overlap in power spectra, phases would need to be controlled in the overlapping portion of the spectrum. In other words, spectral overlap prevents the overlap region from combining spectrally.

Semiconductor diode lasers and fiber lasers are ideal sources for spectral beam combining because of their ease in building in array formats, their high efficiency, and their near-diffraction-limited beam quality from individual elements. Temperature changes can cause wavelength shifts of individual laser emitters. MIT Lincoln Laboratory used a plane back mirror to provide optical feedback so that the spectrum of each element was controlled to be different from the others and was correct for ideal beam combination [6].

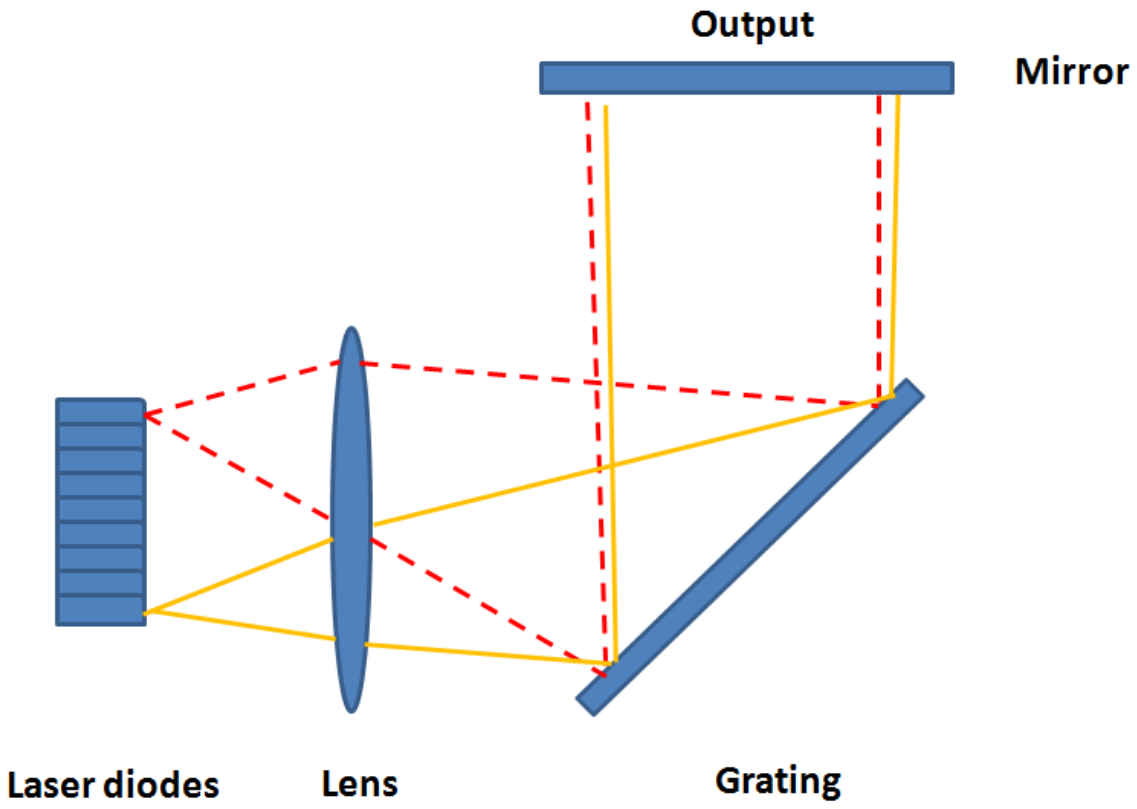

Fig. 2.2 Spectral beam combining with feedback [6]

The configuration of the setup using optical feedback is shown in Fig. 2.2. The lens, grating, and output coupler are common optical elements of the external resonator shared by each of the laser array elements. The facets of laser emitters near the lens side are angle polished or have an antireflection coating to eliminate parasitic lasing. Coaxial propagation of the individual beams is forced by the flat mirror, because the propagation directions of the individual beams are all normal to this mirror. Since the incidence angles on the grating for the beams from each laser emitter differ, the external resonator

selects different wavelengths for each laser emitter as needed to realize codirectional propagation.

Compared with coherent beam combining, spectral beam combining has a broader output spectrum, and this spectrum will become wider as the number of combining elements is increased. Spectral beam combining is unsuitable for applications that require a high coherence laser source. However, for applications that are only concerned with power, spectral beam combining is easier to implement and align than coherent beam combining.

Another advantage of spectral beam combining is its higher tolerance to individual element failure than coherent beam combining. A spectral beam combining system of N elements suffers 1/N power loss if one laser element stops working [7]. However, for coherent beam combining system, this is not the case.

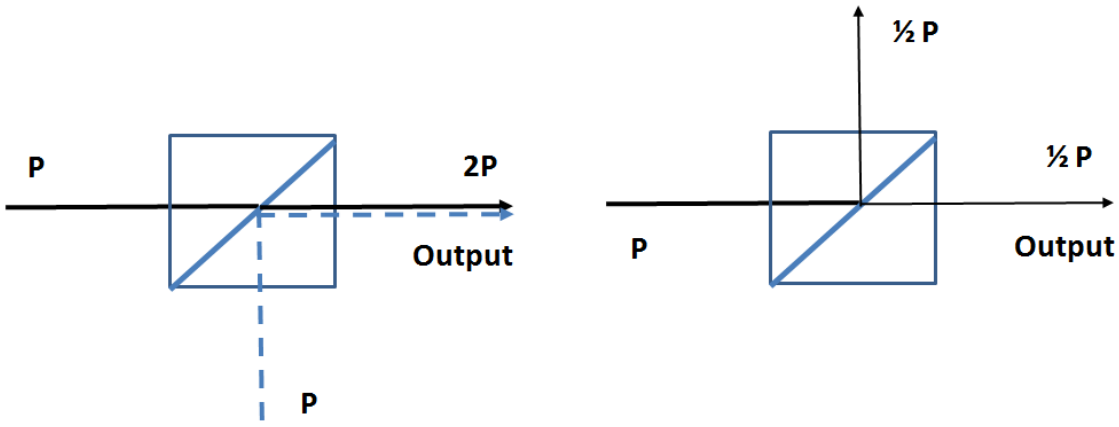

(a) (b)

Fig. 2.3 Effects when one element fails in two-element coherent beam combining (a) no element failure; (b) one element failure

Figure 2.3 shows the beamsplitter coherent beam combining of two elements. If one element fails, the output power would decrease from 2P to ½ P. The power loss is 75% instead of 50%.

Spectral beam combining provides the flexibility to add or remove elements to meet power scaling requirements. Coherent beam combining is more rigid with the number of laser elements and the configuration of the combining systems.

Chapter 3 Common Cavity Coherent Beam Combining

Common cavity coherent beam combining arranges all gain elements in one cavity. Each gain element runs at a moderate power level. The physical separation of gain elements increases the surface to volume ratio compared with using one bulk gain element. All of the gain elements operate with the same spectrum and the relative phases of the elements are controlled such that there is constructive interference. The radiance theorem [8] states that the radiance of an incoherent beam combining system cannot exceed the maximum radiance of a single gain element. Coherent beam combining provides a way of creating a high-radiance laser source which is indispensable for applications such as LIDAR.

Coherent beam combining has been implemented with success in a variety of gain media including semiconductor lasers and fiber lasers. Rare-earth doped fibers have a number of advantages such as high gain, compactness, great stability and flexibility. An ytterbium-doped large-core fiber laser with 1.36 kW continuous-wave output power has been demonstrated by J. Nilsson et al. in 2004 [9].

Several techniques have been proposed to establish mutual coherence across multiple lasers in a common cavity, including the evanescent coupling between waveguides [10], [11], 3-dB coupler arrays [12] and Dammann gratings [13], Talbot self-imaging [14], [15], the self-Fourier principle [16-18], and spatial filtering [19], [20].

Techniques of coherent beam combining can be subdivided into tiled-aperture techniques and filled-aperture techniques. Tiled-aperture architectures, which include Talbot cavities, self-Fourier cavities and spatial filtering cavities, lead to a larger beam size. Filled-aperture architectures, which include 3-dB coupler arrays and Dammann grating cavities, combine multiple beams into a single beam with the same beam size. Detailed analyses of these cavities are presented in Chapter 3.1-3.4.

3.1 Self-Fourier Cavity

The self-Fourier cavity was first proposed and experimentally verified by Corcoran et al. in 2005 [18]. It is achieved by arranging an array of laser gain elements at the input to an external cavity as shown in Fig. 3.1. The electric field amplitude distribution of the fundamental mode of the self-Fourier cavity is equal to its own spatial Fourier transform. It is composed of an array of Gaussian beams with an overall Gaussian envelope as shown in Fig. 3.2.

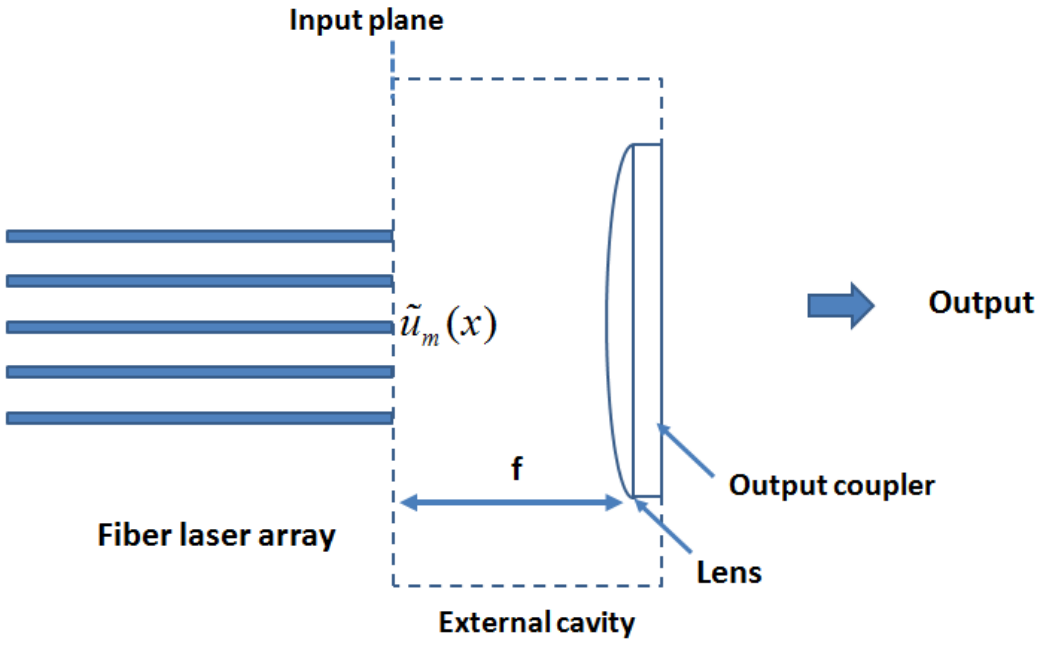

Fig. 3.1 Self-Fourier coherent beam combining cavity

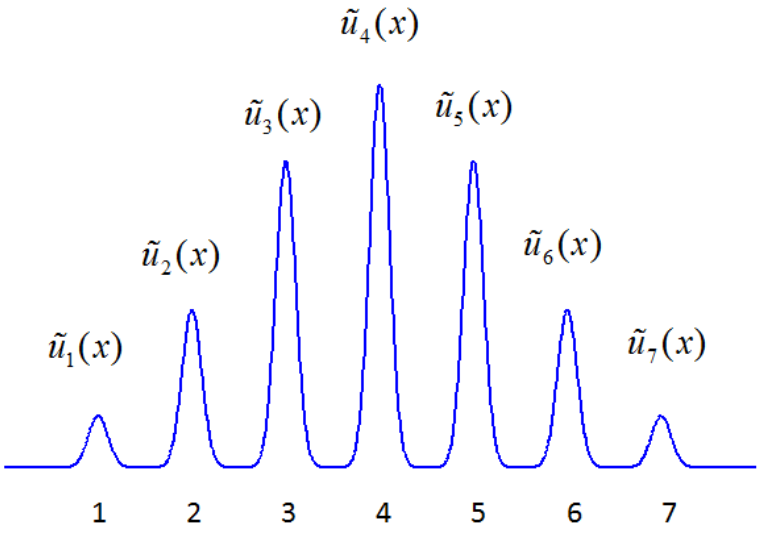

Fig. 3.2 A Self-Fourier function

Each laser gain element is assumed to support only the lowest-order Hermite-Gaussian mode. The electric field of the light exiting the mth gain element $\tilde{u}_m(x)$ is then expressed by a Gaussian beam with a beam waist of ω and a wavelength of λ.

$$\tilde{u}_m(x) = a_m \exp\left[-(x - dm)^2 / \omega^2\right] \tag{3.1}$$

The initial field distribution at the input plane in Fig. 3.1 is given by,

$$f(x) = \sum_{m=-\infty}^{\infty} \tilde{u}_m(x) = a_m \exp\left[-(x - dm)^2 / \omega^2\right] \tag{3.2}$$

The modal analysis begins by evaluating the amplitude coupling from each element of the array to all the elements of the array after propagating one round trip through the external cavity. The receiving field from the mth element is given by,

$$\tilde{v}_m(x) = a_m \sqrt{\pi}\omega \exp\left[-\frac{j2\pi mxd}{\lambda f} - \left(\frac{\pi x\omega}{\lambda f}\right)^2\right] \tag{3.3}$$

The coupling matrix is obtained by evaluating the overlap integral between the receiving field of the nth gain element $\tilde{v}_n(x)$, and the distribution of the mth gain element $\tilde{u}_m(x)$.

$$c_{m,n} = \frac{\int \tilde{u}_m(x)\tilde{v}_n^*(x)dx}{\sqrt{\int \left|\tilde{u}_m(x)\right|^2 dx}\sqrt{\int \left|\tilde{v}_n^*(x)\right|^2 dx}} \tag{3.4}$$

The cavity matrix that describes the round-trip field propagation is written as,

$$M = \left(c_{m,n} e^{j\phi_m}\right) \tag{3.5}$$

ϕ_m is the additional phase delay in the mth gain element. The modal properties of this cavity are obtained by solving the eigenvalue equations. Numerical calculations show that the cavity matrix has only one non-zero eigenvalue and physically the self-Fourier cavity supports only one mode.

3.2 Talbot cavity

The Talbot effect was discovered by Henry Fox Talbot in 1836. When a plane wave is transmitted through a periodic structure, the resulting wave front propagates in a way that it replicates the periodic structure at multiples of a defined distance, known as the Talbot distance.

$$Z_T = \frac{2d^2}{\lambda} \tag{3.6}$$

The parameter d is the structure period and λ is the wavelength of the optical wave. At half the Talbot distance, a self image also occurs and is laterally shifted by half the structure period. At one quarter of the Talbot distance, the self image appears with half the structure period and twice as many patterns are seen.

A Talbot cavity is an external cavity used for coherent beam combining of the output from multiple laser elements arranged in an array. The configuration of a Talbot cavity is shown in Fig. 3.3. The single output mirror of the cavity is positioned at half the Talbot distance from the output facet of the array. Diffractive coupling of array elements based on the Talbot effect is utilized to introduce mode discrimination between array supermodes and thereby ensure modal stability to higher output powers.

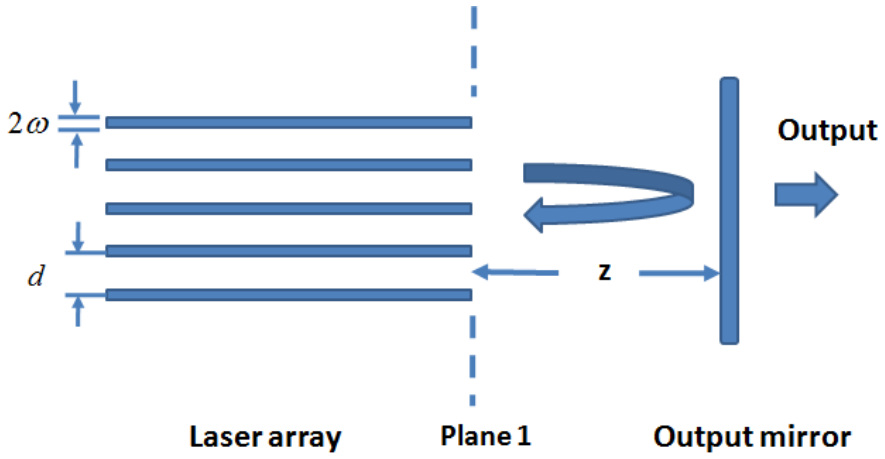

Fig. 3.3 A Talbot coherent beam combining cavity

Each laser gain element is assumed to support only the lowest-order Hermite-Gaussian mode. The electric field of the light exiting the mth array element $\tilde{u}_m(x)$ is expressed by a Gaussian beam with a beam waist of ω and a wavelength of λ.

$$\tilde{u}_m(x) = a_n \exp\left[-(x - dm)^2 / \omega^2\right] \tag{3.7}$$

The coupling coefficients $c_{m,n}$ correspond to the amount of field of the mth gain element that couples into the nth gain element after propagating from plane 1 back to the same plane. This is determined by calculating an overlap integral between the receiving mode of the nth gain element and the distribution of the mth gain element mode [21].

$$c_{m,n} = \frac{\sqrt{\pi}\omega \exp(4\pi i z / \lambda)}{\sqrt{\pi\omega^2 + iz\lambda}} \exp\left[\frac{-\pi d^2 (m-n)^2}{2(\pi\omega^2 - i\lambda z)}\right] \tag{3.8}$$

The cavity matrix that describes the round-trip field propagation is written as,

$$M = \left(c_{m,n} e^{j\phi_m}\right) \tag{3.9}$$

ϕ_m is the additional phase delay in the m^{th} gain element. The modal properties of this cavity are obtained by solving the eigenvalue equations. If the propagation distance equals one full Talbot distance ($z=1/2\ Z_T$), the field consists of a linear superposition of an in-phase and out-of-phase mode. If the propagation distance equals one-half Talbot distance ($z=1/4\ Z_T$), the fundamental mode is the out-of-phase mode.

3.3 Michelson cavity

The configuration of the Michelson cavity is shown in Fig. 3.4. This cavity coherently combines the power generated by the gain elements into a single beam exiting the output arm. A beam block ensures that no light returns from the upper arm of the beam splitter.

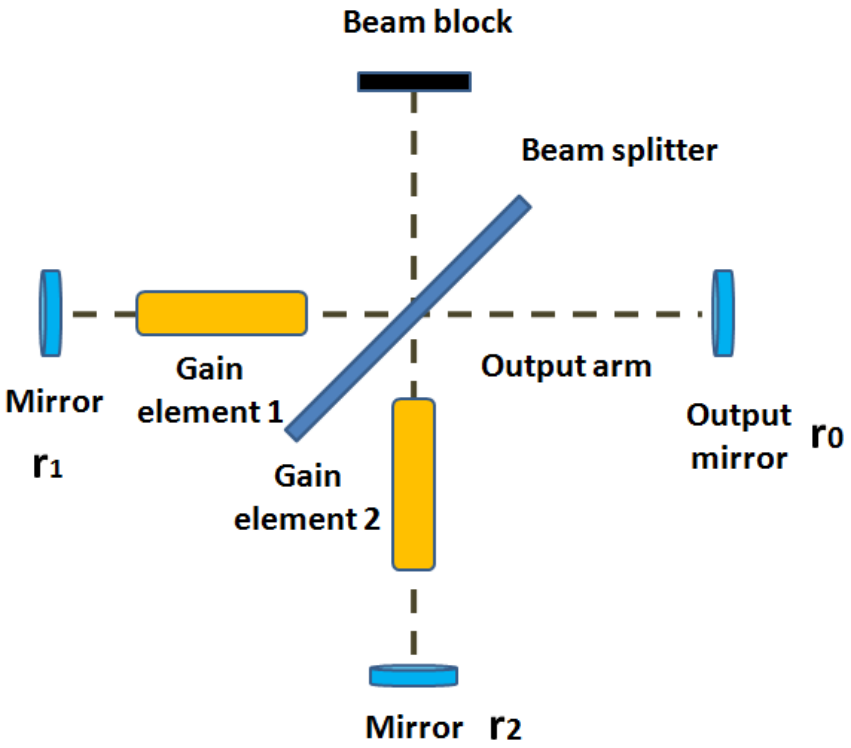

Fig. 3.4 A Michelson beam combining cavity [12].

A beamsplitter splits one incoming beam into two outgoing beams with a fixed phase relationship. According to the time reversal property, two incoming beams with the same fixed phase relationship are combined perfectly by the beamsplitter (Fig. 3.5).

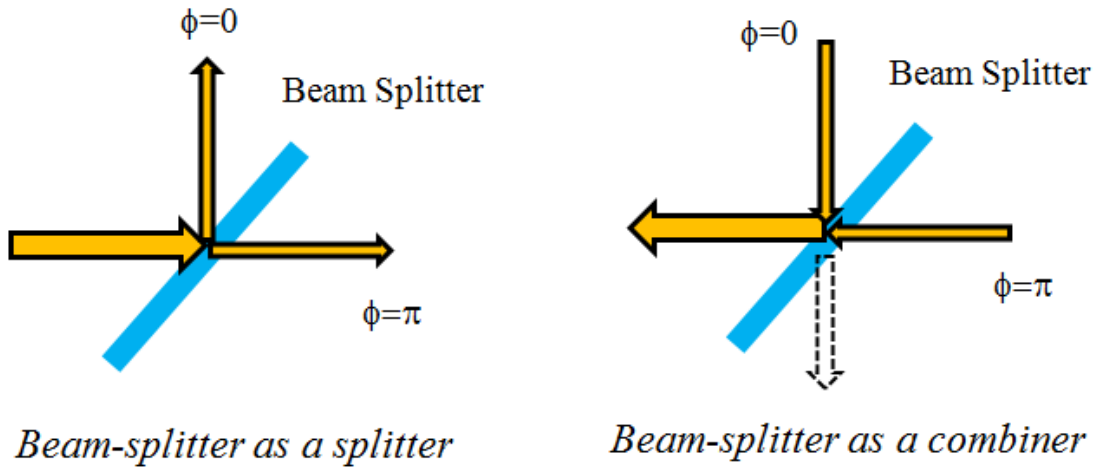

Fig. 3.5 Beamsplitter as a splitter or a combiner

M. Khajavikhan performed a detailed analysis on the modal properties of the Michelson cavity [12]. The modal properties are obtained by solving the eigenvalue equations that describe the light propagation inside the resonator. We assume that the beams start their propagation from mirror r_1 and r_2. They acquire phase retardation as they travel through the gain elements.

$$\Phi = \begin{pmatrix} e^{j(\varphi_1/2)} & 0 \\ 0 & e^{j(\varphi_2/2)} \end{pmatrix} \tag{3.10}$$

They are redirected by the beamsplitter into the upper and output arms according to the beamsplitter scattering matrix.

$$S = \begin{pmatrix} 1/\sqrt{2} & j/\sqrt{2} \\ j/\sqrt{2} & 1/\sqrt{2} \end{pmatrix} \tag{3.11}$$

The beam in the output arm is reflected back by the output mirror r_0 and is subsequently redirected by the beamsplitter into the gain elements according to the transpose scattering matrix. The beam in the upper arm is absorbed by the beam block.

$$R = \begin{pmatrix} r_0 & 0 \\ 0 & 0 \end{pmatrix} \tag{3.12}$$

The beams acquire additional phase retardation as they travel once more through the gain elements. They are reflected by mirror r_1 and r_2 respectively and return to the starting points. The round-trip matrix of the cavity is the product of all these individual matrices.

$$M = \Phi S^T R S \Phi = \begin{pmatrix} \frac{1}{2} r_0 e^{j\phi_1} & \frac{j}{2} r_0 e^{j\frac{(\phi_1+\phi_2)}{2}} \\ \frac{j}{2} r_0 e^{j\frac{(\phi_1+\phi_2)}{2}} & -\frac{1}{2} r_0 e^{j\phi_2} \end{pmatrix} \tag{3.13}$$

By solving the equation $\Lambda X = MX$, the eigenvalues Λ and eigenvectors X of this matrix can be obtained. The matrix M has only one non-zero eigenvalue.

$$\lambda = -jr_0 e^{j\frac{(\phi_1+\phi_2)}{2}} \sin(\frac{\phi_2 - \phi_1}{2}) \tag{3.14}$$

The Michelson cavity with a beam block supports only one supermode. The fiber-based 3-dB coupler cavity as shown in Fig. 3.6 has the same modal properties.

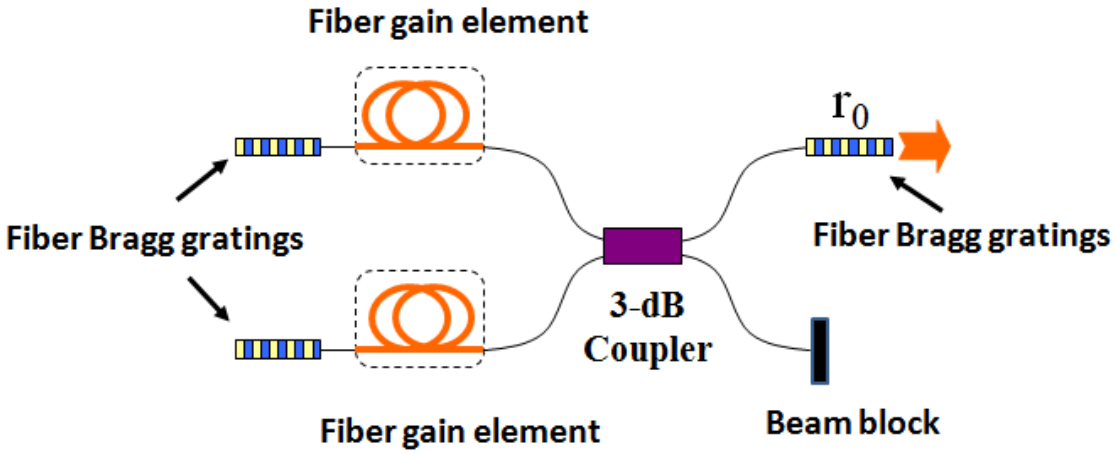

Fig. 3.6 The configuration of a 3-dB coupler cavity

3.4 Dammann grating cavity

A Dammann grating effectively acts as a multi-port beamsplitter. The configuration of the Dammann grating cavity is shown in Fig. 3.7. The cavity coherently combines the power generated by three gain elements into a single beam exiting the output mirror. The modes of the Dammann grating cavity can be calculated by solving the eigenvalue equations that represent the propagation of a given field through one complete cavity round trip. The round-trip cavity matrix is given by [12],

$$M = \frac{1}{3} r_0 \begin{pmatrix} e^{j\frac{4\pi}{3}} e^{j\phi_1} & e^{j\frac{2\pi}{3}} e^{j\frac{\phi_1+\phi_2}{2}} & e^{j\frac{4\pi}{3}} e^{j\frac{\phi_1+\phi_3}{2}} \\ e^{j\frac{2\pi}{3}} e^{j\frac{\phi_1+\phi_2}{2}} & e^{j\phi_2} & e^{j\frac{2\pi}{3}} e^{j\frac{\phi_2+\phi_3}{2}} \\ e^{j\frac{4\pi}{3}} e^{j\frac{\phi_1+\phi_3}{2}} & e^{j\frac{2\pi}{3}} e^{j\frac{\phi_3+\phi_2}{2}} & e^{j\frac{4\pi}{3}} e^{j\phi_3} \end{pmatrix} \tag{3.15}$$

The cavity matrix is a unity-rank matrix and has only one non-zero eigenvalue.

$$\lambda = \frac{r_0}{3} e^{j\frac{4\pi}{3}} e^{j\phi_2} \left(e^{j(\phi_1-\phi_2)} + e^{j\frac{2\pi}{3}} + e^{j(\phi_3-\phi_2)} \right) \tag{3.16}$$

The Dammann grating resonator is inherently single-mode and the power is evenly extracted from all the gain elements.

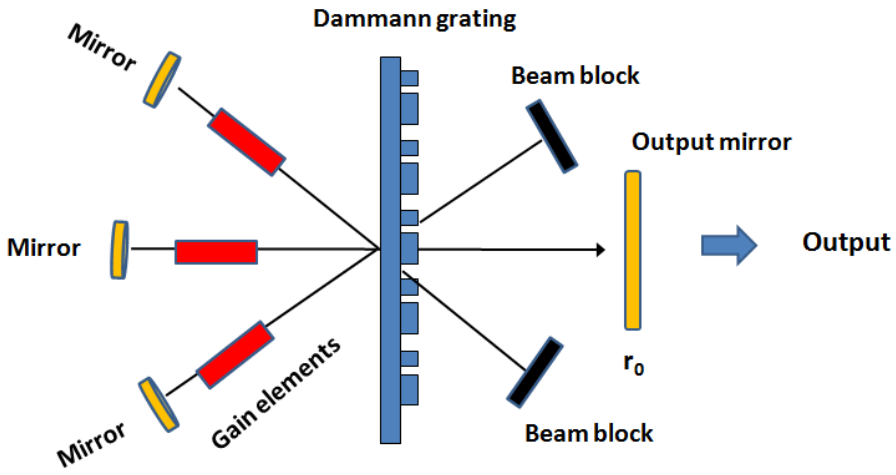

Fig. 3.7 A Dammann grating beam combining cavity

Chapter 4 Analysis of Path Length Sensitivity in Coherent Beam Combining by Spatial Filtering

This chapter provides a detailed theoretical analysis on path length sensitivity in coherent combining architectures based on Fourier-plane spatial filtering. We perform a cold cavity analysis on the spatially filtered two-gain-element cavity shown in Fig. 4.1. In particular, we seek to determine the loss behavior of the supermodes as a function of cavity length errors in each of the laser arms. Unlike the beam splitter and Dammann grating cavities, the spatially filtered cavity naturally contains multiple supermodes, where the loss of each supermode is a function of the filter design. Architectures containing more gain elements are discussed and analyzed in Chapter 4.2.

In Chapter 4.1, we develop an analytical model of the modes in a two-laser system. We demonstrate that the modal behavior of the spatially filtered cavity is very different from that of the 3-dB cavity. In Chapter 4.2 we explore the cavity modes through a computer simulation. The simulation is used to test the validity of the analytical model, as well as to explore more complex filtering operations and cavities containing multiple lasers. We also address the question of the optimal filter design to increase path length phase error tolerance while preserving modal discrimination. Chapter 4.3 presents a comparison of the Michelson cavity and the spatial filtering cavity with respect to modal properties. Chapter 4 is written based on the paper [22].

4.1 Theory

The modes of a laser cavity can be easily calculated by solving the eigenvalue equations that describe the propagation of a given field through one complete cavity round trip. For simplicity, we choose a two-laser system where the spatial filter is represented by a single aperture in the center of the filter (or Fourier) plane. In addition, since the array consists of a linear array of sources, a one-dimensional analysis is employed. Thus, we seek to determine the eigenvectors and eigenvalues of the 2 x 2 coupling matrix corresponding to a single round-trip propagation of the light field out of and back into the single-spatial-mode gain elements, and including the round-trip phase difference $\varphi_1 - \varphi_2$ between gain channels imposed by the path length error $2\Delta z$ at the end mirrors. In actual practice, this phase error can result from a variety of sources. For example, when fibers are used as gain media, small changes in the fiber length or index can result in significant phase errors between gain channels.

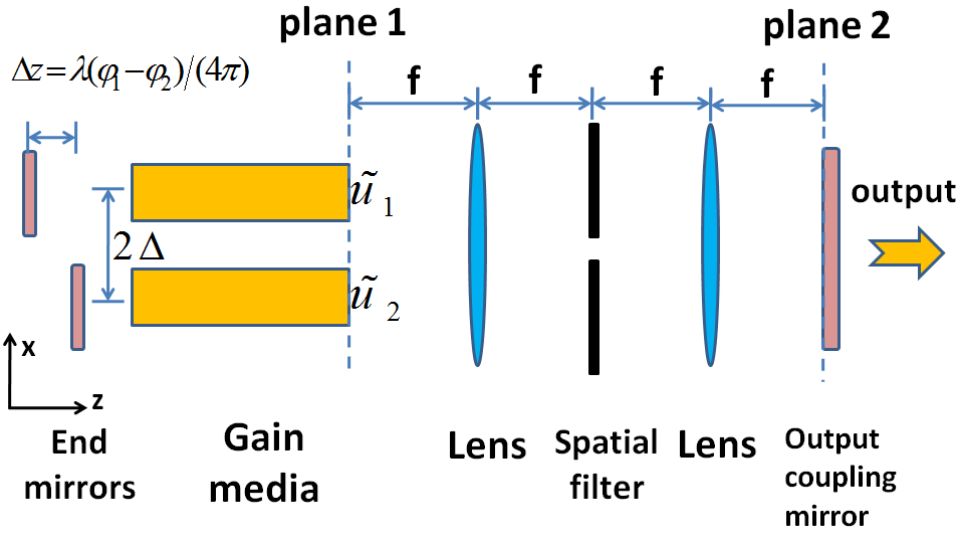

Fig. 4.1 Two beam combining with a Gaussian filter [22].

B. Tiffany performed a cold cavity analysis on the spatially filtered cavity shown in Fig. 4.1. As shown in Fig. 4.1, the two gain elements are separated laterally by 2Δ in the cavity. Each gain element is assumed to support only the lowest-order Hermite-Gaussian mode. The electric field of the light exiting the i^{th} gain element $\tilde{u}_i(x)$ is then expressed by a Gaussian beam with a beam waist of ω and a wavelength of λ. The light fields $\tilde{u}_1(x)$ and $\tilde{u}_2(x)$ exiting the two gain elements are given by:

$$\tilde{u}_1(x) = \sqrt{\frac{1}{\omega}\sqrt{\frac{2}{\pi}}}\exp\left[-(x-\Delta)^2/\omega^2\right] \tag{4.1}$$

and

$$\tilde{u}_2(x) = \sqrt{\frac{1}{\omega}\sqrt{\frac{2}{\pi}}}\exp\left[-(x+\Delta)^2/\omega^2\right] \tag{4.2}$$

The constants before the exponential term are chosen to normalize the total power. The two lenses that comprise the afocal imaging system each have a focal length of *f*. A

spatial filter with Gaussian transmittance is assumed for mathematical simplicity. The amplitude transmittance of the filter is given by

$$t = \exp(-x^2/a^2) \tag{4.3}$$

where *a* corresponds to the spatial width of the filter.

The round-trip ABCD propagation matrix of the 4*f* system (from Plane 1 to Plane 2 and back to Plane 1) is [23]

$$\begin{pmatrix} A & B \\ C & D \end{pmatrix} = \begin{pmatrix} 0 & f \\ -\frac{1}{f} & 0 \end{pmatrix} \begin{pmatrix} 1 & 0 \\ -\frac{j\lambda}{\pi a^2} & 1 \end{pmatrix} \begin{pmatrix} 0 & f \\ -\frac{1}{f} & 0 \end{pmatrix} \begin{pmatrix} 0 & f \\ -\frac{1}{f} & 0 \end{pmatrix} \begin{pmatrix} 1 & 0 \\ -\frac{j\lambda}{\pi a^2} & 1 \end{pmatrix} \begin{pmatrix} 0 & f \\ -\frac{1}{f} & 0 \end{pmatrix}$$
$$= \begin{pmatrix} 1 & j\frac{2f^2\lambda}{\pi a^2} \\ 0 & 1 \end{pmatrix} \tag{4.4}$$

This ABCD matrix can be used to calculate the diffraction pattern $\tilde{v}(x)$ of any initial distribution $\tilde{u}(x)$ through the equation (4.5) [23]:

$$\tilde{v}(x) = \int_{-\infty}^{\infty} \tilde{K}(x,\xi)\tilde{u}(\xi)d\xi \tag{4.5}$$

where

$$\tilde{K}(x,\xi) = \sqrt{\frac{j}{B\lambda}} \exp\left[\frac{-j\pi}{B\lambda}\left(Ax^2 - 2x\xi + D\xi^2\right)\right] \tag{4.6}$$

In our case, the four elements of the ABCD matrix are given by A=1, B=$j2f^2\lambda/(\pi a^2)$, C=0 and D=1. The round trip distributions $\tilde{v}_1$ and $\tilde{v}_2$, produced by $\tilde{u}_1(x)$ and $\tilde{u}_2(x)$ respectively, become

$$\tilde{v}_1(x) = \frac{2^{1/4}\pi^{-1/4}\omega^{-1/2}}{\sqrt{1+\delta}} \exp\left[-\frac{(x-\Delta)^2}{(1+\delta)\omega^2}\right] \tag{4.7}$$

$$\tilde{v}_2(x) = \frac{2^{1/4}\pi^{-1/4}\omega^{-1/2}}{\sqrt{1+\delta}} \exp\left[-\frac{(x+\Delta)^2}{(1+\delta)\omega^2}\right] \tag{4.8}$$

$$\delta = \frac{2f^2\lambda^2}{\pi^2\omega^2 a^2} \tag{4.9}$$

Note that

$$\int_{-\infty}^{\infty} \left|\tilde{v}_1(x)\right|^2 dx = \int_{-\infty}^{\infty} \left|\tilde{v}_2(x)\right|^2 dx = \frac{1}{\sqrt{1+\delta}} \tag{4.10}$$

Thus the remaining total power from a single gain element after one round trip is given by Eq. (4.10) and is only a function of δ.

The coupling matrix coefficients c_{ij} correspond to the amount of field of the ith gain element that couples into the jth gain element after propagating from plane 1 back to the same plane. This is determined by calculating an overlap integral between the receiving mode of the jth gain element, $\tilde{u}_j(x)$, and the distribution of the ith gain element mode after one round trip, $\tilde{v}_i(x)$ for i,j = (1,2):

$$c_{11} = \int_{-\infty}^{\infty} \tilde{u}_1^*(x)\tilde{v}_1(x)dx = \frac{1}{\sqrt{1+\delta/2}} \tag{4.11}$$

$$c_{21} = \int_{-\infty}^{\infty} \tilde{u}_2^*(x)\tilde{v}_1(x)dx = \exp\left[-\frac{4\Delta^2}{(2+\delta)\omega^2}\right] \Big/ \sqrt{1+\delta/2} \tag{4.12}$$

$$c_{12} = \int_{-\infty}^{\infty} \tilde{u}_1^*(x)\tilde{v}_2(x)dx = \exp\left[-\frac{4\Delta^2}{(2+\delta)\omega^2}\right] \Big/ \sqrt{1+\delta/2} \tag{4.13}$$

$$c_{22} = \int_{-\infty}^{\infty} \tilde{u}_2^*(x)\tilde{v}_2(x)dx = \frac{1}{\sqrt{1+\delta/2}} \tag{4.14}$$

The round-trip coupling matrix corresponding to the entire cavity must account for the additional phase delays that occur between output coupling mirrors and plane 1. We express these round-trip phases as φ_1 and φ_2 corresponding to the first and second gain element respectively. Thus based on equations (4.11)-(4.14), the total cavity matrix can be expressed as,

$$M = \begin{pmatrix} c_{11}e^{j\varphi_1} & c_{12}e^{j\varphi_1} \\ c_{21}e^{j\varphi_2} & c_{22}e^{j\varphi_2} \end{pmatrix} \tag{4.15}$$

By solving the equation $\Lambda X = MX$, the eigenvalues Λ and eigenvectors X of this matrix can be obtained. In particular, we are interested in the elemental eigenvalues λ_i contained in the matrix Λ, where the power loss L to the i^{th} mode is given by $L = 1 - |\lambda_i|^2$. We find

$$\lambda_{1,2} = \frac{\exp(j\bar{\varphi})}{\sqrt{1+\delta/2}}\left[\cos(\varphi/2) \pm \sqrt{\exp\left[-\frac{8\Delta^2}{(2+\delta)\omega^2}\right] - \sin^2(\varphi/2)}\right] \tag{4.16}$$

where $\bar{\varphi} = (\varphi_1 + \varphi_2)/2$, $\varphi = \varphi_1 - \varphi_2$ .The corresponding normalized eigenvectors are

$$v_1 = \left\{ \frac{R_+}{\sqrt{R_+^2 + 1}}, \frac{1}{\sqrt{R_+^2 + 1}} \right\} \tag{4.17}$$

$$v_2 = \left\{ \frac{R_-}{\sqrt{R_-^2 + 1}}, \frac{1}{\sqrt{R_-^2 + 1}} \right\} \tag{4.18}$$

where

$$R_{+,-} = \left[-j\sin(\varphi/2) \pm \sqrt{\exp\left[-\frac{8\Delta^2}{(2+\delta)\omega^2} \right] - \sin^2(\varphi/2)} \right] \exp\left(j\varphi/2 \right) \exp\left[\frac{4\Delta^2}{(2+\delta)\omega^2} \right] \tag{4.19}$$

The matrix has two sets of eigenvectors with associated eigenvalues, corresponding to the two supermodes supported by this cavity. When there is no phase error (φ=0 in Eq. 4.19), the two eigenvectors in equations 4.17 and 4.18 represent the typical symmetric and antisymmetric modes.

Of particular interest is the condition that if

$$\sin^2(\varphi/2) \geq \exp\left[-\frac{8\Delta^2}{(2+\delta)\omega^2} \right] \tag{4.20}$$

then $|\lambda_1| = |\lambda_2|$, which indicates that the two supermodes have the same power loss per round trip. The practical implication of this is that the two modes will have the same gain in this path length error range, and thus simple gain clamping will not be able to suppress multi-mode oscillations. Of course, the phase of the eigenvalues does change in this path length error range, making the frequencies of the modes distinct.

4.2 Simulation and Analysis

The cavity analysis in Chapter 4.1 assumes a Gaussian transmittance spatial filter to permit an analytical solution. It is of interest, however, to calculate the cavity modes under more general filtering conditions. A computer model was developed for this purpose, where the matrix coefficients of Eq. 4.15 were calculated numerically using scalar diffraction theory. An eigenvector solver was then employed to determine the corresponding eigenvectors and eigenvalues. Fig. 4.2 compares the analytical solution of the eigenvalues from Eq. 4.16 to the computer model. Obviously the close fit indicates that there is good agreement between the two. The parameters used in the analysis include inter-element half spacing (Δ= 0.566mm), beam width (ω= 0.400mm), focal length (f= 40mm), Gaussian transmittance filter width (a= 0.01155mm) and wavelength (λ=1μm).

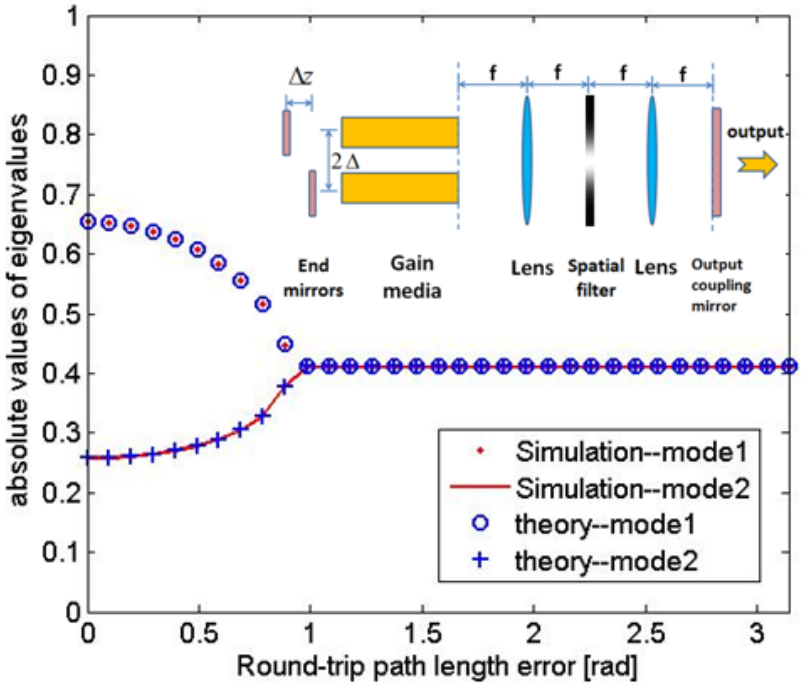

(a)

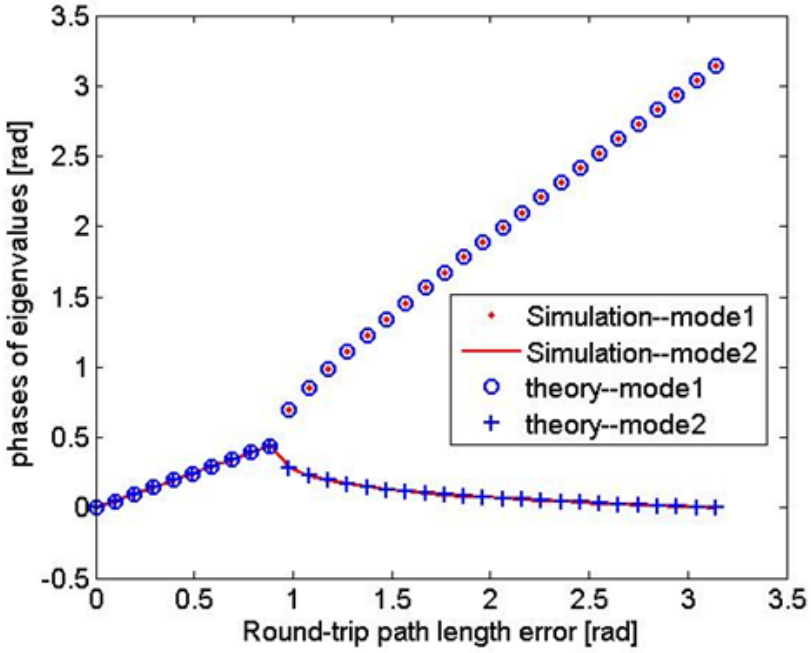

(b)

Fig. 4.2 Eigenvalues vs. phase error of the coupled cavity using a Gaussian spatial filter. (a) Eigenvalue magnitude. (b) Eigenvalue phase.

The most obvious feature in Fig. 4.2 is the critical point predicted by Eq. 4.20. Path length errors less than this critical value produce eigenvectors with dissimilar magnitudes but identical phases, whereas path length errors greater than this point produce eigenvalues with identical magnitudes and differing phases.

The consequences of the above behavior are profound. Most simple laser cavities achieve single spatial mode operation by providing loss mechanisms to higher-order modes, ensuring that only the lowest-order mode will reach the lasing threshold. This strategy indeed works for the present laser cavity in the region to the left of the coalescence point in Fig. 4.2. However, our analysis indicates that gain cannot be used to discriminate between supermodes when path length errors are present that are greater than the value given by Eq. 4.20 because the losses between the two modes become identical. In principle, the phase difference on the right side of the coalescence point can be used to differentiate the modes as well, since this phase difference represents two dissimilar optical path lengths, and results in slightly different oscillation frequencies. It is conceivable that a narrow band spectral filter such as a Fabry-Perot could be used as a discrimination element. However, changes in path length errors would require active tuning of the filter, reducing some of the appeal of a common cavity architecture.

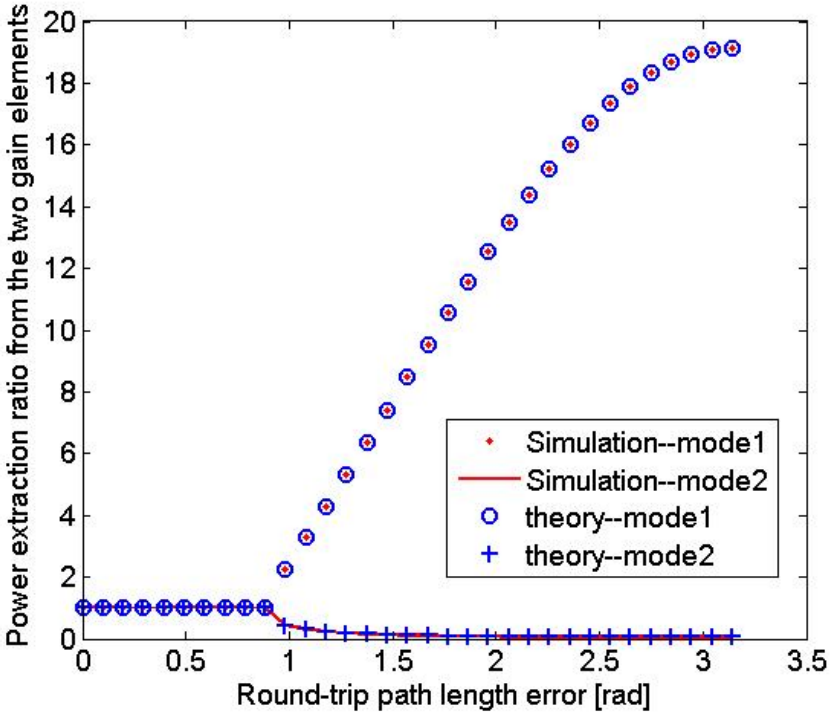

Fig. 4.3 Power extraction ratio from the two gain elements

A second interesting characteristic of this cavity is seen from Eqs. 4.17 and 4.18 describing the distribution of the field in the two gain arms. The power extraction ratio is defined as the ratio of the power extracted from gain element 1 to the power extracted from gain element 2. It can be seen that both supermodes extract the same amount of powers from the two gain elements in small phase error region and different amount of powers in large phase error region. In fact, to the right of the coalescence point the two supermodes can be distinguished from one another by the power distribution in the gain elements. One supermode extracts a larger amount of power from gain element 1 while the other supermode extracts more power from gain element 2 (Fig. 4.3).

The computer model was used to explore more complex filtering operations. The first test replaced the Gaussian transmittance filter with a hard-clipping aperture. This aperture is of practical interest, as it is much simpler to implement. Interestingly, the qualitative behavior of this filter was almost identical to the Gaussian filter, with the curves having very similar shapes to Fig. 4.2.

Next, we explored the consequences of spatial filter size. Of course, we expected larger spatial filters to have reduced loss. This is apparent from Eq. 4.9 where increased values of *a* result in smaller values of δ and consequently larger total round-trip powers from Eq. 4.10. Figure 4.4 shows the absolute values of the eigenvalues for two single-hole apertures of different size. The smaller aperture in figure 4.4(a) produces a fundamental mode eigenvalue of 0.9 and a second-mode eigenvalue of 0.73, corresponding to a round trip power loss $1 - |\lambda|^2$ of 19% and 47% respectively. Enlarging the filter reduces the losses to both modes, resulting in a power loss of 6.5% and 15% respectively. Perhaps more interestingly, the point of coalescence moves to the left, indicating that the region where simple balanced gain can be used to discriminate the modes has reduced. This shift in the coalescence point is also apparent from Eq. 4.20 for Gaussian spatial filters. Thus, there is an apparent tradeoff between mode loss and phase error tolerance.

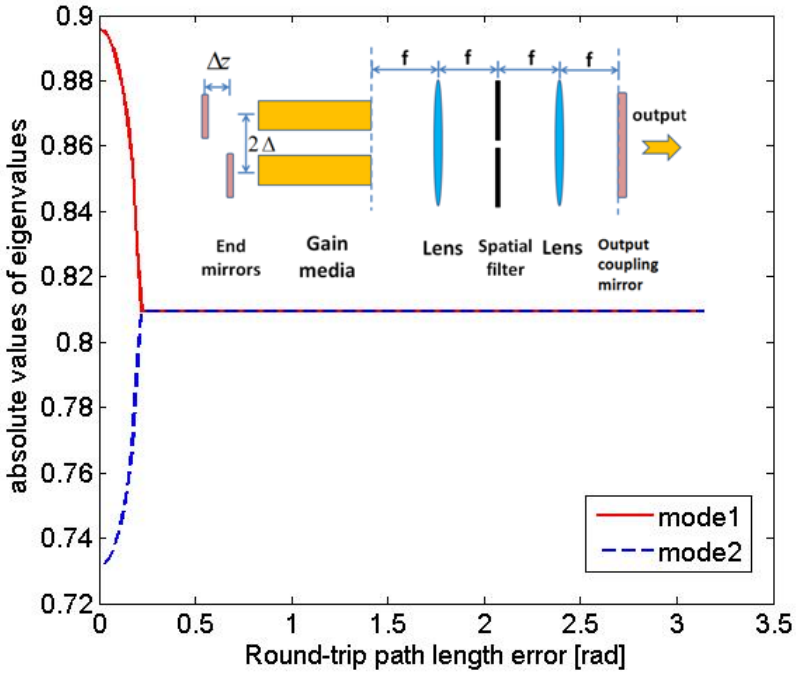

(a)

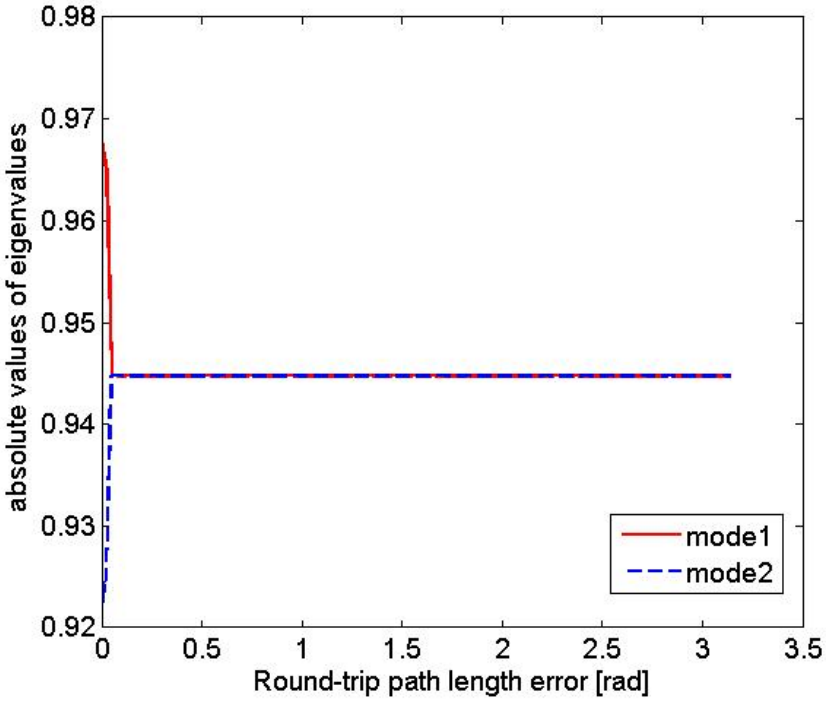

(b)

Fig. 4.4 Magnitude of the two modal eigenvalues for (a) smaller single-hole spatial filter and (b) larger single-hole filter.

We performed an *ad hoc* exploration of the filter design space by simulating a variety of filter types, including multiple-hole apertures and absorption spots. The ideal filter would have a low fundamental mode loss while simultaneously maintaining a wide phase error tolerance. We concluded that in general, inverse filters satisfy these two properties better than traditional apertures. Here inverse filtering refers to a filter that has a small absorbing area in an otherwise transparent region. The simplest form of inverse filter places an absorbing spot at a particular location, as shown in the inset of Fig. 4.5. Compared to a single-hole aperture (Fig. 4.4a), the single blocking spot has a smaller fundamental mode loss (solid curve) and a wider phase error tolerance region. Increased modal discrimination can be achieved by using smaller apertures or larger blocking spots, but is inevitably accompanied by a simultaneous increase in cavity loss.

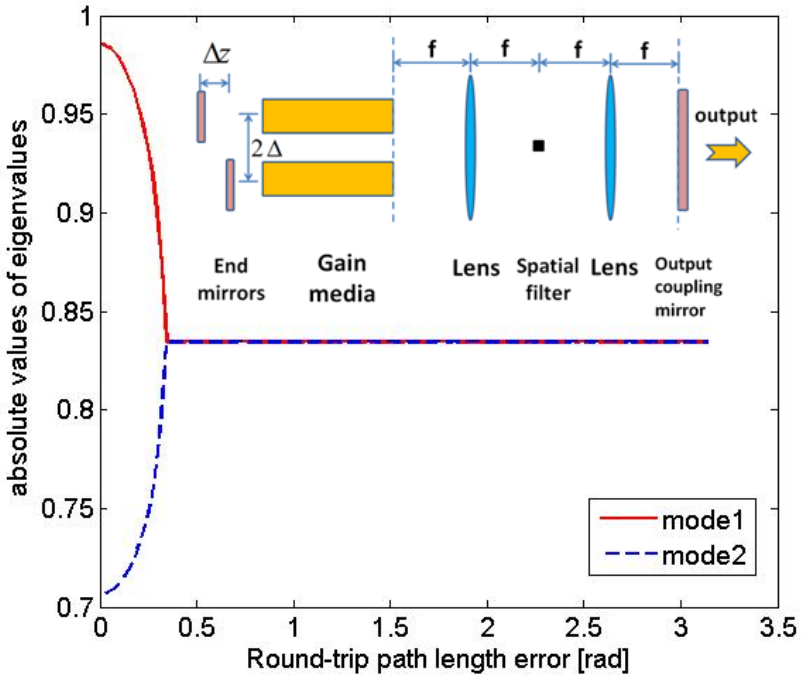

Fig. 4.5 Mode curves for an absorbing spot filtering

An analytical exploration of inverse filtering can be performed by studying a cavity with an inverse Gaussian filter. The amplitude transmittance of this filter is given by

$$t = 1 - \exp(-x^2/a^2) \tag{4.21}$$

The round trip distributions $\tilde{v}_1$ and $\tilde{v}_2$, produced by $\tilde{u}_1(x)$ and $\tilde{u}_2(x)$ respectively, become

$$\tilde{v}_1(x) = \sqrt{\frac{1}{\omega}\sqrt{\frac{2}{\pi}}}\exp\left[-(x-\Delta)^2/\omega^2\right] - \frac{2^{1/4}\pi^{-1/4}\omega^{-1/2}}{\sqrt{1+\delta}}\exp\left[-\frac{(x-\Delta)^2}{(1+\delta)\omega^2}\right] \tag{4.22}$$

$$\tilde{v}_2(x) = \sqrt{\frac{1}{\omega}\sqrt{\frac{2}{\pi}}}\exp\left[-(x+\Delta)^2/\omega^2\right] - \frac{2^{1/4}\pi^{-1/4}\omega^{-1/2}}{\sqrt{1+\delta}}\exp\left[-\frac{(x+\Delta)^2}{(1+\delta)\omega^2}\right] \tag{4.23}$$

$$\text{where} \quad \delta = \frac{2f^2\lambda^2}{\pi^2\omega^2a^2} \tag{4.24}$$

Similarly, the coupling matrix coefficients c_{ij} are determined by calculating an overlap integral between the receiving mode of the j^{th} gain element, $\tilde{u}_j(x)$, and the distribution of the i^{th} gain element mode after one round trip, $\tilde{v}_i(x)$ for i,j = (1,2):

$$c_{11} = \int_{-\infty}^{\infty}\tilde{u}_1^*(x)\tilde{v}_1(x)dx = 1 - \frac{1}{\sqrt{1+\delta/2}} \tag{4.25}$$

$$c_{21} = \int_{-\infty}^{\infty}\tilde{u}_2^*(x)\tilde{v}_1(x)dx = \exp\left[-\frac{2\Delta^2}{\omega^2}\right] - \exp\left[-\frac{4\Delta^2}{(2+\delta)\omega^2}\right]\Big/\sqrt{1+\delta/2} \tag{4.26}$$

$$c_{12} = \int_{-\infty}^{\infty}\tilde{u}_1^*(x)\tilde{v}_2(x)dx = \exp\left[-\frac{2\Delta^2}{\omega^2}\right] - \exp\left[-\frac{4\Delta^2}{(2+\delta)\omega^2}\right]\Big/\sqrt{1+\delta/2} \tag{4.27}$$

$$c_{22} = \int_{-\infty}^{\infty} \tilde{u}_2^*(x)\tilde{v}_2(x)dx = 1 - \frac{1}{\sqrt{1+\delta/2}} \tag{4.28}$$

Based on Eqs. 4.25-4.28, the total cavity matrix can be expressed as,

$$M = \begin{pmatrix} c_{11}e^{j\varphi_1} & c_{12}e^{j\varphi_1} \\ c_{21}e^{j\varphi_2} & c_{22}e^{j\varphi_2} \end{pmatrix} \tag{4.29}$$

Again, φ_1 and φ_2 correspond to the round-trip phases from the first and second gain element respectively. As before, the eigenvalues of this matrix can be obtained by solving the equation $\Lambda X = MX$,

$$\lambda_{1,2} = \exp(j\bar{\varphi})\left[\cos(\varphi/2)*\left(1-\frac{1}{\sqrt{1+\delta/2}}\right)\right] \pm \exp(j\bar{\varphi}) \sqrt{\left[\exp\left(-\frac{2\Delta^2}{\omega^2}\right) - \frac{\exp\left(-\frac{4\Delta^2}{(2+\delta)\omega^2}\right)}{\sqrt{1+\delta/2}}\right]^2 - \left(1-\frac{1}{\sqrt{1+\delta/2}}\right)^2 \sin^2(\varphi/2)} \tag{4.30}$$

where $\bar{\varphi} = (\varphi_1 + \varphi_2)/2$, $\varphi = \varphi_1 - \varphi_2$.

We compare inverse Gaussian filters with Gaussian filters based on three aspects: 1) fundamental mode loss ($1-|\lambda_1|^2$) with no phase error, 2) width of phase tolerance region measured by the distance from origin to coalescence point, and 3) mode discrimination,

defined as

$$G_2 / G_1 = \frac{(1/\lambda_2)^2}{(1/\lambda_1)^2} = \frac{\lambda_1^2}{\lambda_2^2} \tag{4.31}$$

λ_i describes the field attenuation per round trip of the i_{th} supermode and $1/\lambda_i^2$ is the required gain to run the i_{th} supermode. Thus the mode discrimination is defined as the ratio of the required gain of the two supermodes.

We plot phase tolerance and mode discrimination as a function of fundamental mode loss in figure 4.6 and in figure 4.7 respectively. It is clearly shown that in the low loss region (fundamental mode loss < 0.5), the inverse Gaussian filter has superior performance compared to the Gaussian filter with regard to both phase tolerance and mode discrimination.

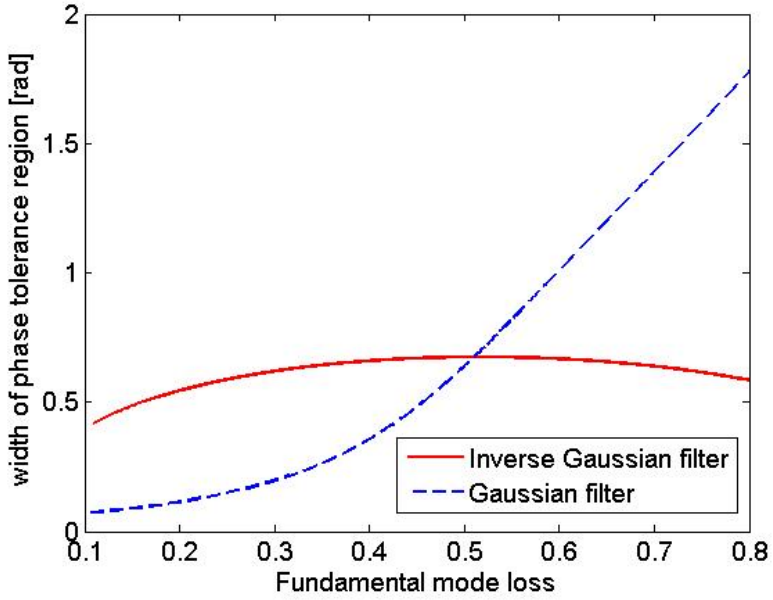

Fig. 4.6 Phase tolerance vs. fundamental mode loss. Solid curve: Inverse Gaussian filter; dashed curve: Gaussian filter.

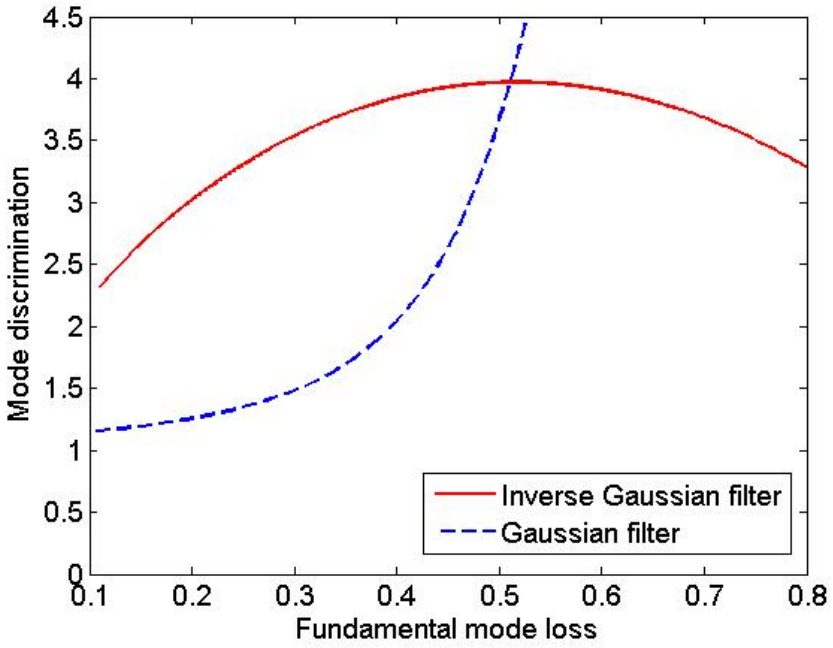

Fig.4.7 Mode discrimination vs. fundamental mode loss. Solid curve: Inverse Gaussian filter; dashed curve: Gaussian filter.

Although a study of two gain media is important to understand the basic principles, laser designers are generally interested in using larger array sizes. To explore the effects of including additional gain elements, we simulated the three element case with a smaller single-hole aperture in Fig. 4.8 and a larger single-hole aperture in Fig. 4.9. The phase error is introduced by varying the path length of the central gain element. The intriguing point is that the mode loss curves no longer coalesce. Instead, there is a *turning point* where all the loss curves become flat. In addition, before this flattening point, all the modes have a fixed power extraction ratio from the three gain elements. For example, for the fundamental mode (mode1) in figure 4.9(a), the ratio of powers extracted from the three elements is 1.04:1:1.04; and for mode 3, this ratio is 1:4.16:1. After this point,

however, both modes (mode 1 and 3) tend to extract an increasing amount of power from one or two of the three elements.

Another point to notice is that there is a flat curve across the entire region in Figs. (4.8a) and (4.9a). The independence of this solution to central element path length error is simply a consequence of the fact that this eigenmode contains no power in the central element. Such a mode is not ideal for beam combining because the central element gain is left unused. In contrast, the fundamental mode in Fig. 4.9(a) is more desirable, not only because it has lower loss than the other modes, but also extracts energy fairly uniformly from all three elements (1.04:1:1.04). However, we notice that this condition only is satisfied for a limited range of phase errors (from origin to the turning point). After the turning point, the modes (mode 1 and 3) tend to extract an increasing amount of power from one or two of the three elements.

The fact that the three-element case has no coalescence point may make it easier to select a mode by means of gain clamping. Comparing Fig. 4.8 and Fig. 4.9, we find that increasing the aperture size lowers the losses of all the modes and the three curves become closer to each other, indicating a decrease in modal discrimination.

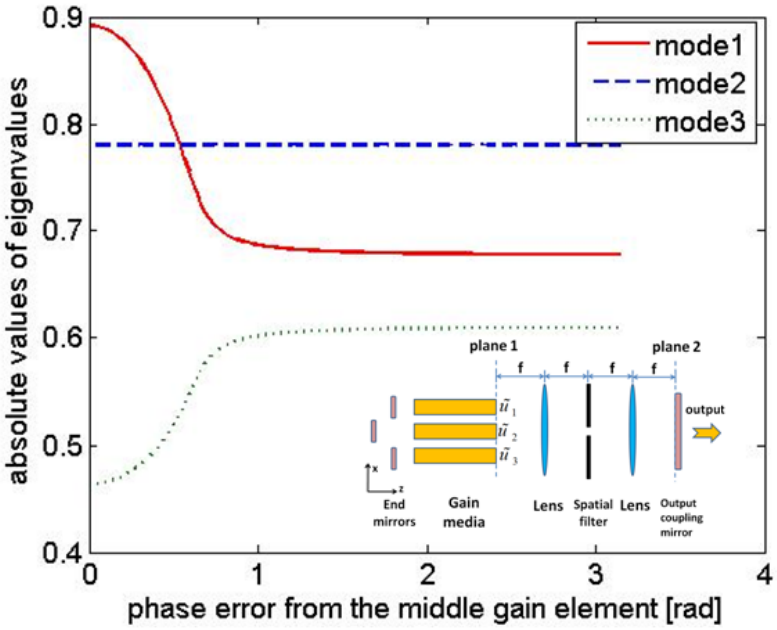

(a)

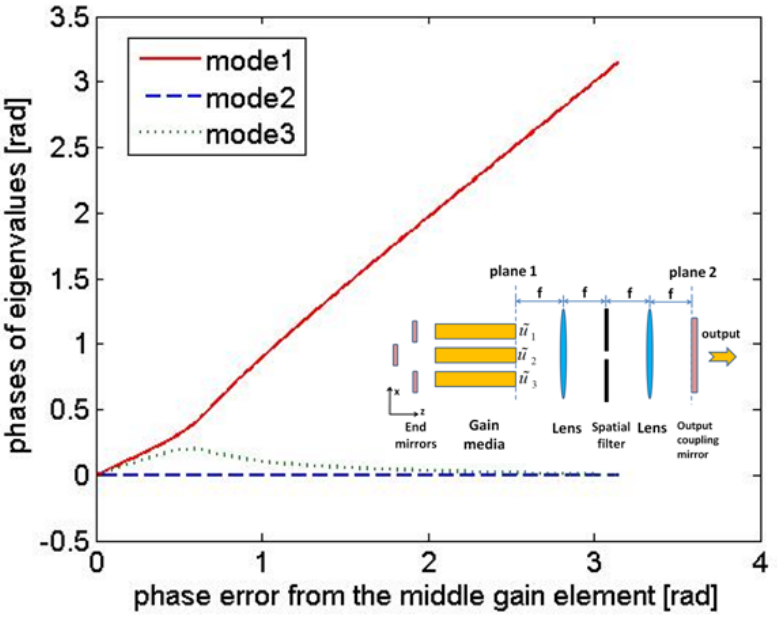

(b)

Fig. 4.8 Mode curves of three gain element cavity: small aperture
(a) Eigenvalue magnitude; (b) Eigenvalue phase.

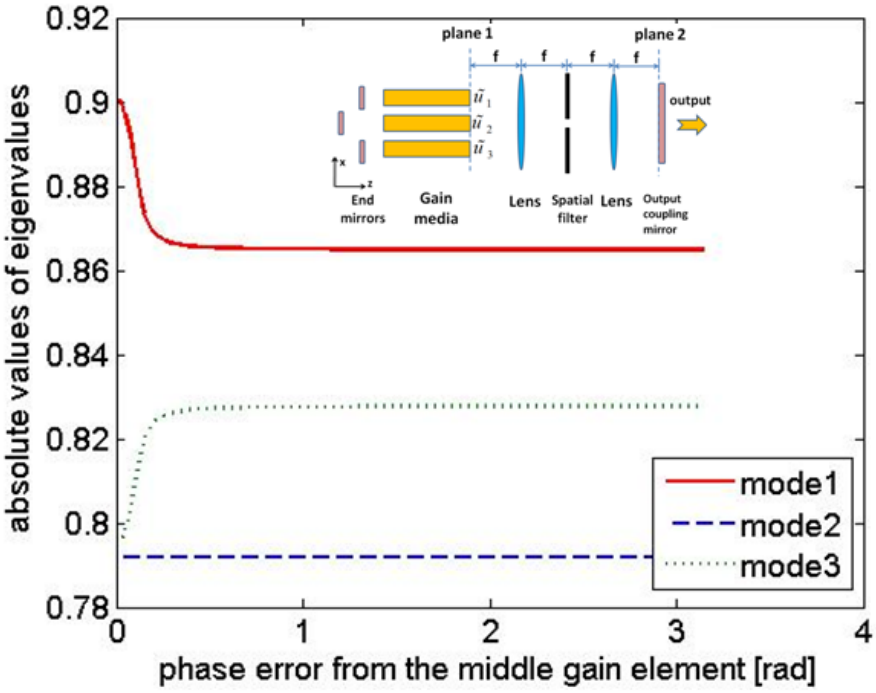

(a)

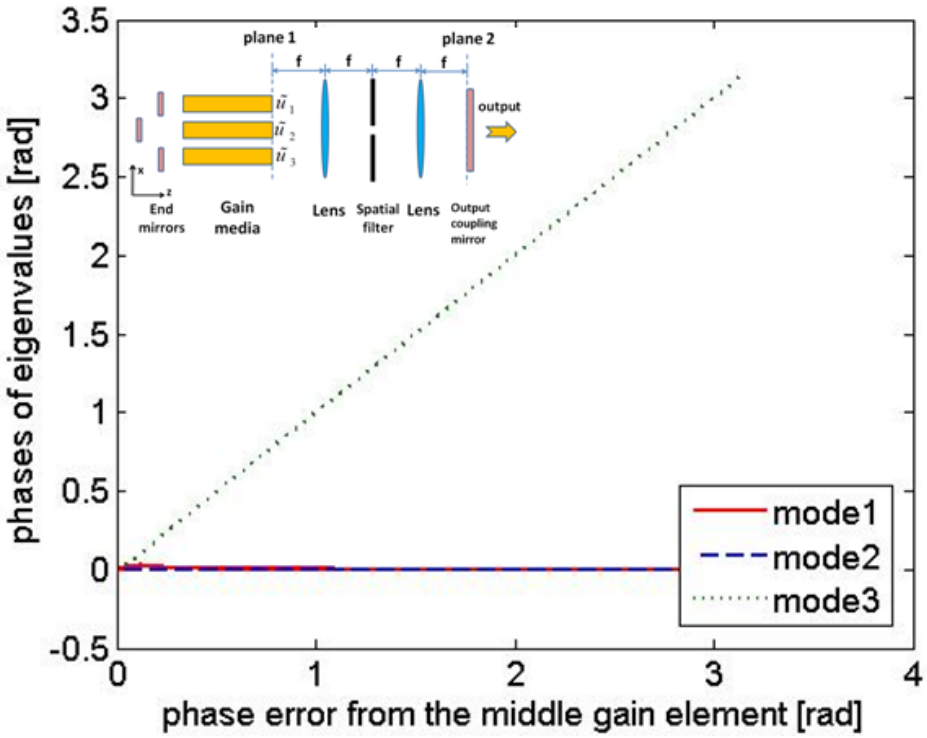

(b)

Fig.4.9 Mode curves of three gain element cavity: large aperture
(a) Eigenvalue magnitude; (b) Eigenvalue phase.

4.3 Comparison with the Michelson Cavity

The modal properties of the Michelson cavity with a beam block are analyzed in Chapter 3.3. The cavity matrix is given by [12],

$$M = \Phi S^T R S \Phi = \begin{pmatrix} \frac{1}{2} r_0 e^{j\phi_1} & \frac{j}{2} r_0 e^{j\frac{(\phi_1+\phi_2)}{2}} \\ \frac{j}{2} r_0 e^{j\frac{(\phi_1+\phi_2)}{2}} & -\frac{1}{2} r_0 e^{j\phi_2} \end{pmatrix} \tag{4.32}$$

The matrix M has only one non-zero eigenvalue.

$$\lambda = -j r_0 e^{j\frac{(\phi_1+\phi_2)}{2}} \sin(\frac{\phi_2 - \phi_1}{2}) \tag{4.33}$$

The Michelson cavity with a beam block supports only one supermode. If the beam block is replaced by a mirror (Fig. 4.10), the cavity matrix becomes [12],

$$M2 = \begin{pmatrix} \frac{1}{2}(r_0 - r_r) e^{j\phi_1} & \frac{j}{2}(r_0 + r_r) e^{j\frac{(\phi_1+\phi_2)}{2}} \\ \frac{j}{2}(r_0 + r_r) e^{j\frac{(\phi_1+\phi_2)}{2}} & -\frac{1}{2}(r_0 - r_r) e^{j\phi_2} \end{pmatrix} \tag{4.34}$$

The matrix M2 has two non-zero eigenvalues [12].

$$\lambda_1 = \frac{-j}{2} e^{j\frac{\phi_1+\phi_2}{2}} \left((r_0 - r_r)\sin(\frac{\Delta\phi}{2}) + \sqrt{(r_0 - r_r)^2 \sin^2(\frac{\Delta\phi}{2}) + 4 r_0 r_r} \right) \tag{4.35}$$

$$\lambda_2 = \frac{-j}{2} e^{j\frac{\phi_1+\phi_2}{2}} \left((r_0 - r_r)\sin(\frac{\Delta\phi}{2}) - \sqrt{(r_0 - r_r)^2 \sin^2(\frac{\Delta\phi}{2}) + 4 r_0 r_r} \right) \tag{4.36}$$

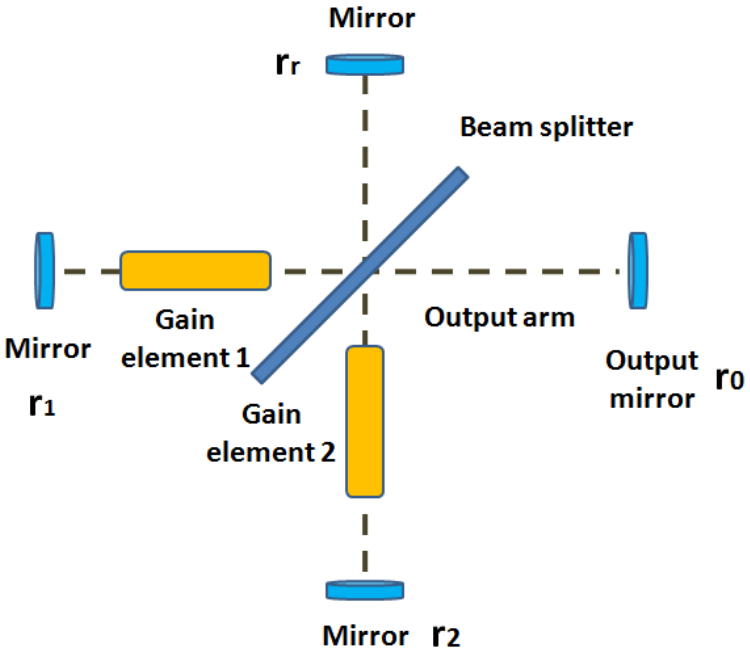

Fig. 4.10 A four-port Michelson beam combining cavity

The mode loss curves are plotted in Fig. 4.11 and Fig. 4.12.

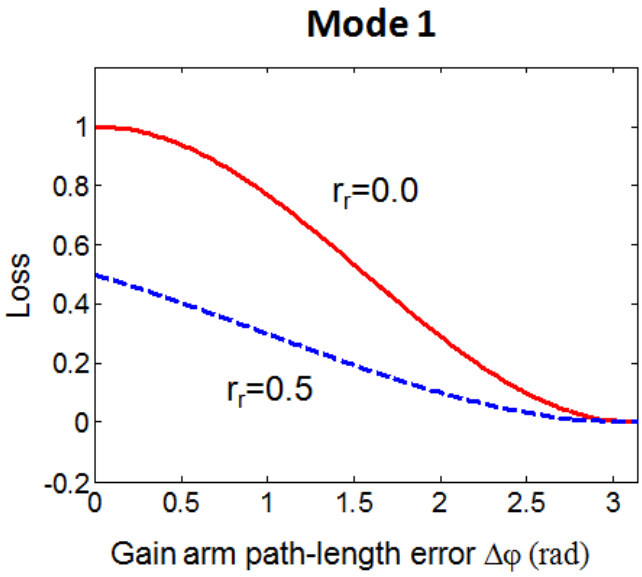

Fig. 4.11 The loss curve of mode 1

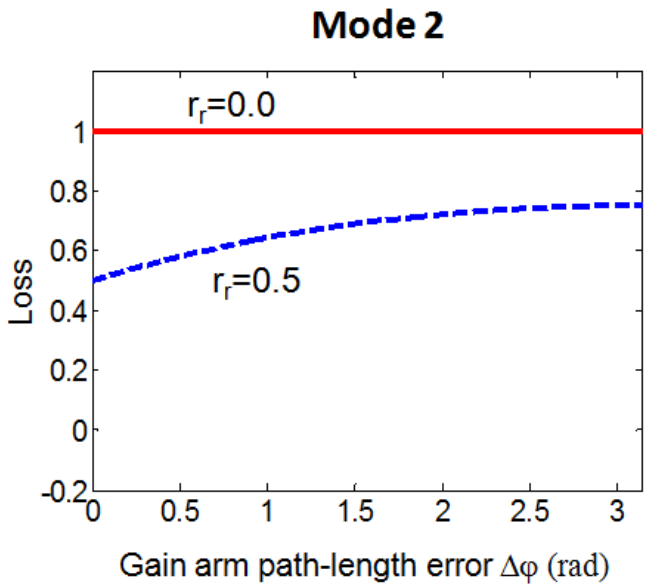

Fig. 4.12 The loss curve of mode 2

The red solid curves correspond to the Michelson cavity with a beam block (Fig. 3.4). Mode 2 always has a complete loss. In other words, the cavity supports only one supermode. The blue dashed curves correspond to the four-port Michelson cavity (Fig. 4.10). This cavity supports two supermodes and virtually all path length errors result in dissimilar eigenvalue magnitudes (except for the zero phase error point).

Chapter 5 Experiment on Path Length Sensitivity in Coherent Beam Combining by Spatial Filtering

5.1 Experiment apparatus design

This chapter is written based on the paper [24]. The measurement of the modal properties of coupled arrays requires special care. To observe the properties predicted by Eqs. 4.16-4.19, we must design a laser cavity that consists of two separate gain arms, maintain precise control over the relative path lengths between the gain arms, and devise a method to accurately measure the complex field distribution predicted by Eq. 4.17. In addition, the total optical path length of both cavities must be identical to within a few hundred micrometers to ensure that changes in wavelength do not substantially affect the relative phases between gain arms. To accomplish this, we have chosen to spatially superimpose the two gain arms of Fig. 4.1 into a common beam in the left half of the cavity in Fig. 5.1 by polarization multiplexing. The two gain channels have been encoded into vertical and horizontal polarization states, and thus share the same optical path through the gain material, left side half-wave plates, and end mirror in Fig. 5.1. Any variation in physical path length affects the two polarization states equally and makes this part of the cavity extremely stable. In addition, the phase relationship between the two channels can be conveniently adjusted by the two half-wave plates by birefringence. Initially the fast axis of one wave plate is aligned with the slow axis of the other wave plate, and the wave plates are perpendicular to the optical axis of the cavity. In this case, the two half wave

plates introduce zero path length difference to the two beam channels. However, tilting the half-wave plates around their fast or slow axes changes the retardation of each plate and thus introduces a controllable path length difference between the two beam channels [25]. This configuration provides highly accurate control of the relative path length error while preserving the overall path length balance.

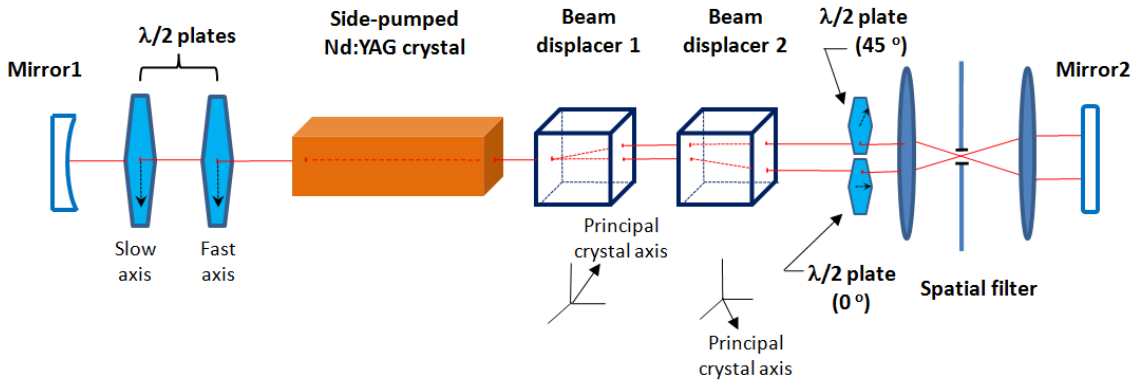

Fig. 5.1 Experiment setup for spatial filtering coherent beam combining [24].

The right-hand side of the cavity in Fig. 5.1 contains the spatial filter required for coherent coupling. Since spatial filtering is based on applying selective loss to the interference pattern in the Fourier plane of a lens, polarization multiplexing cannot be used in this half of the cavity (since orthogonal polarizations do not interfere in the correct manner). Hence, the polarization multiplexed beam exiting the gain crystal is split into two linearly polarized beams by two beam displacers. Each beam displacer is made of high optical grade calcite. One polarization goes through the first beam displacer directly while the orthogonal polarization is shifted laterally by double refraction. The

two orthogonally polarized beams exit this first displacer parallel to each other. Note that the second beam displacer is rotated 90 degrees with respect to the first one, so that the beam that was shifted laterally by the first displacer goes through the second displacer directly whereas the beam that went through the first displacer directly now receives a lateral shift by the second displacer. In this way, not only do the two polarizations separate twice as far, but the balance in optical path lengths of the two beams is preserved.

Continuing to the right, the two displaced beams pass through separate half-wave plates. The principal axis of the upper half-wave plate is oriented at 45 degrees with respect to the vertically polarized upper beam, allowing the wave plate to rotate the state of polarization to horizontal. The principal axis of the lower half-wave plate is oriented parallel to the horizontally polarized lower beam and thus the wave plate does not affect its polarization. However, since the two half-wave plates were obtained from the same original piece of birefringent material, their overall optical phase delays are approximately the same and the optical path lengths of the two cavities remain balanced.

The final section of the cavity contains a conventional spatial filter followed by an end mirror. The spatial filter consists of an afocal imaging system with an aperture or blocking filter in the Fourier plane of the first lens. We have chosen to use blocking filters consisting of thin tungsten wires (2.7 μm and 5 μm diameter) to reduce the overall loss to the cavity. The width of central lobe is 22.4 μm, and the wire covers part of one

lobe. A piezoelectric controller is used for fine position adjustment of the filter. The concave mirror m_1 on the left hand side has 97.5% reflectivity at 1064nm and the plane mirror m_2 on the right hand side has 99% reflectivity at 1064nm. The 1% doped Nd:YAG crystal is 5mm*5mm*50mm in dimension. The crystal is pumped by an 808 nm laser diode bar with 19 individual units and 20% fill factor. The diode bar is temperature controlled at 20 degrees Celsius.

The cavity properties can be assessed using a variety of techniques. The relative loss between supermodes (corresponding to the magnitude of the eigenvalues) can be assessed by measuring the threshold current for a particular path length phase error and matching this threshold value by inserting calibrated attenuators into a cavity with no path length error. The oscillation frequency difference between two simultaneously lasing supermodes (corresponding to the phase difference between the two eigenvalues) can be measured using RF beating techniques. Finally, the amplitude and phase distribution of a particular supermode can be assessed by two methods. In the first method, the far-field intensity pattern of the light exiting the right-hand side of the cavity is evaluated to determine the phase relationship between the lasing channels. However, it can be difficult to determine both the amplitude and phase independently from a far field intensity measurement. An alternative and more accurate method consists of measuring the polarization state of the multiplexed signal exiting the left-hand side of the cavity. This measurement is equivalent to an interferometric measurement between the two channels. Unpolarized light corresponds to the presence of both supermodes, whereas elliptically

polarized light can be analyzed (by an external cavity quarter-wave plate and a polarizer) to determine the amplitude of each gain arm and the phase.

5.2 Experimental results

As a first test of the coupled laser cavity, we observed the far-field lasing behavior with no phase error between the two laser channels. Accordingly, we adjusted the two quarter-wave plates on the left side of the cavity to present a minimum path length error, and recorded the far-field patterns of the light exiting the right hand side of the cavity. We first noticed that removing the filter produced a single Gaussian-like pattern with no visible interference. The absence of interference fringes indicates that, without external coupling, the two channels lased incoherently. When the wire blocking filter was placed in the cavity, the cavity was induced to lase in one of two supermodes, as shown in the far-field patterns of Figs. 5.2 and 5.3. The high contrast interference fringes indicate that the two laser channels are highly coherent, and the location of the peaks indicates which supermode is excited. With the blocking filter in the first location, the in-phase supermode of Fig. 5.2 was observed; moving the blocking filter slightly produced the out-of-phase supermode seen in Fig. 5.3. By way of definition, the term *fundamental* mode refers to the mode that has the least loss (and hence the lowest lasing threshold). Depending on the location of the wire, this fundamental mode can be either an in-phase supermode or an out-of-phase supermode.

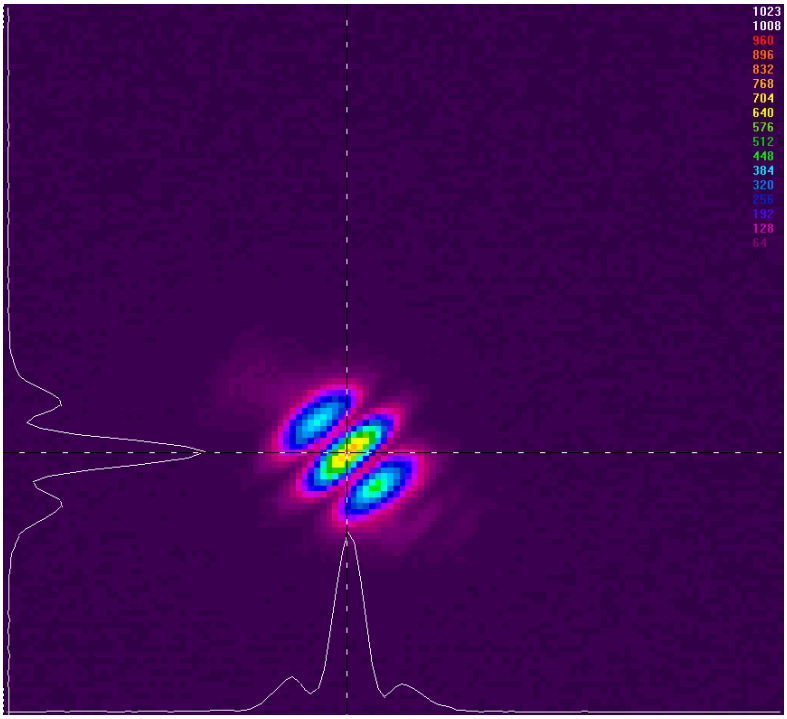

Fig. 5.2 Image of the diffraction pattern from the in-phase supermode

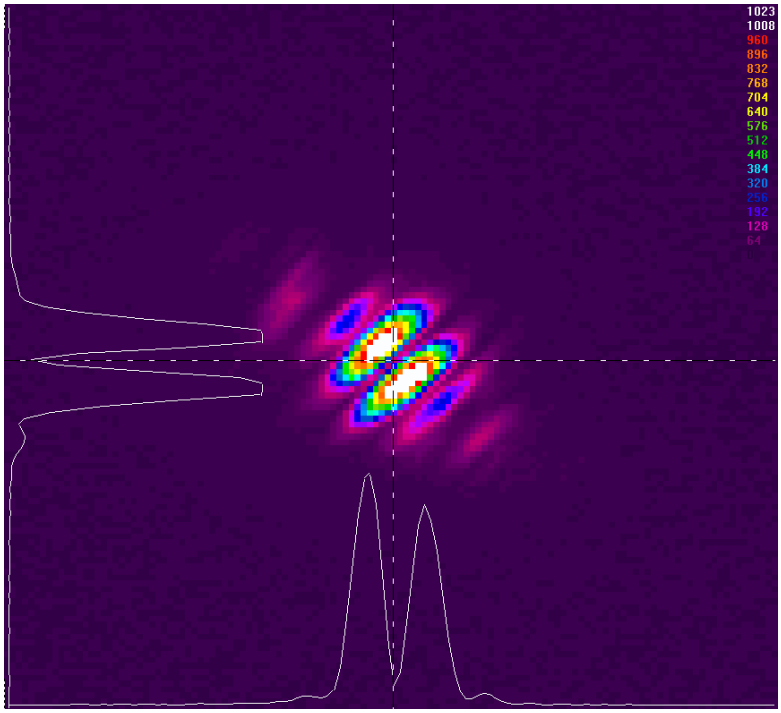

Fig. 5.3 Image of the diffraction pattern from the out-of-phase supermode

As an alternative measure of the supermode state, the polarization of the output beam on the left hand side was measured using a quarter wave plate, a polarizer and a photodetector connected to an oscilloscope. With a path length error of zero, a null could always be found by rotating the quarter wave plate and polarizer to the proper position. This proves that the cavity was oscillating in a single supermode, as predicted by theory.

Next, quantitative measurements were made of the cavity loss as a function of path length error when the spatial filter was adjusted to promote the out-of-phase mode. The resulting data are plotted in Fig. 5.4 along with a plot of the theoretical supermode loss $L_i = 1 - |\lambda_i|^2$. Rather than use the analytical theory, we have plotted the results from a numerical model that accurately represents the effects of the hard-clipping blocking filter. One obvious feature of the curve is the critical point predicted by the analytical theory in Eq. 4.20. This point separates the small and large path length error regions. In the small path length error region, the two supermodes have dissimilar phase-error loss, and only the less lossy supermode can lase. In the large path length error region, both supermodes have the same loss and have an equal chance of lasing. In our experiment, we have seen cases in this region where both supermodes lase simultaneously (resulting in an incoherent state) or alternatively where the supermodes change randomly between the even-order and odd-order supermodes. In Fig. 5.4 we show the far-field patterns as insets in these two regions, where the small path length error region is shown to lase in an out-of-phase supermode, and the large path length region is shown as an incoherent state.

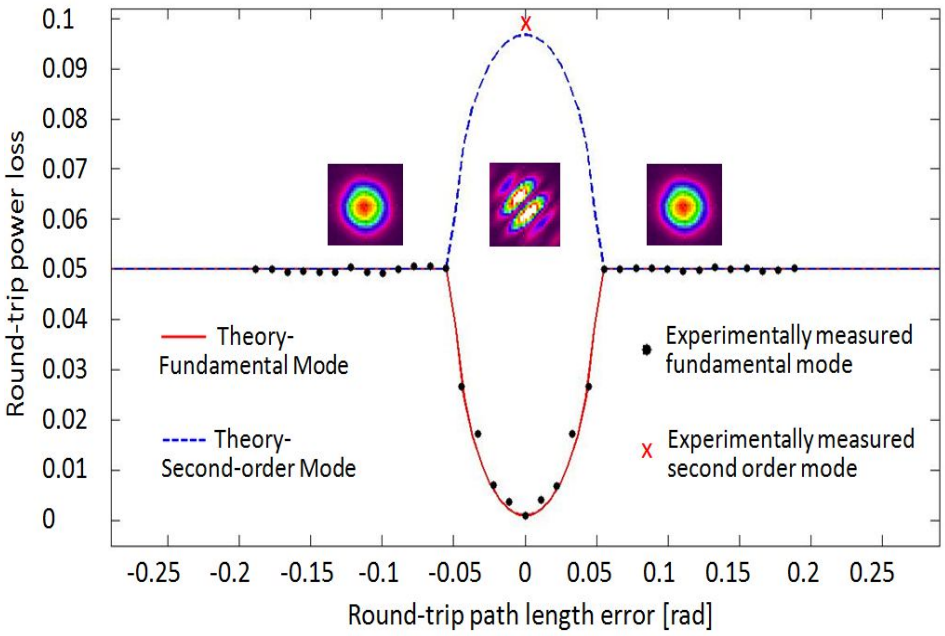

Fig. 5.4 Phase-error loss vs. path length error (out-of-phase fundamental supermode)

When the path length error is zero, the two supermodes are linearly polarized in the left-hand side of the cavity. Thus, a Brewster-angle polarizer inside the cavity can suppress the fundamental supermode while adding negligible loss to the second-order supermode. It is thus possible to accurately measure the loss of the second-order supermode at this point. We plot this data point in Fig. 5.4, showing the maximum modal discrimination.

Figs. 5.5 and 5.6 show the experimentally measured magnitude ratio and relative phase of the two components of the out-of-phase supermode compared with our numerical theory. These values are similar to those given in equations 4.17, 4.18 and 4.19 for a Gaussian-shaped aperture. These measurements were made in the small phase error regime where there was sufficient discrimination to ensure single-mode operation. The magnitudes and

phases were measured using the polarization method described above. The two components of the fundamental supermode were seen to have the same magnitude ratio regardless of the path length error. However, the phase relationship between channels was seen to change with path length error. When the path length error was zero, the two laser channels differed in phase by π. Non-zero path length errors resulted in a departure from this phase state.

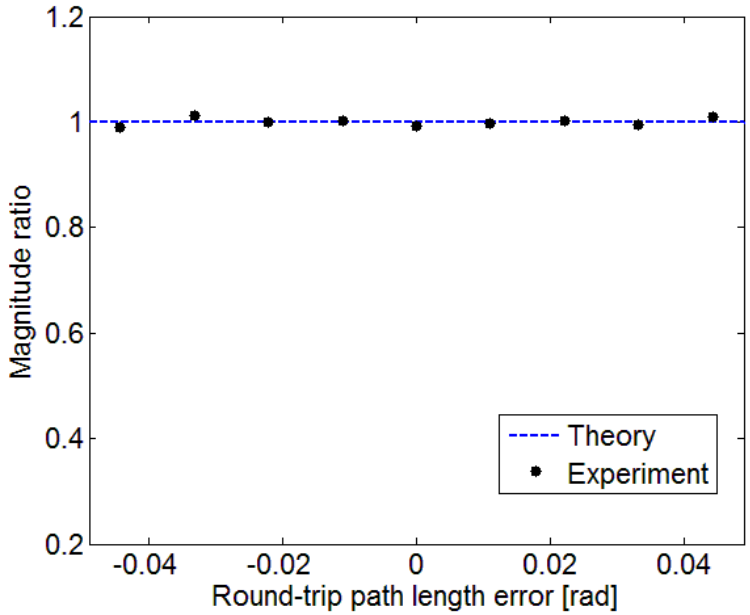

Fig. 5.5 Magnitude ratio of fundamental supermode components

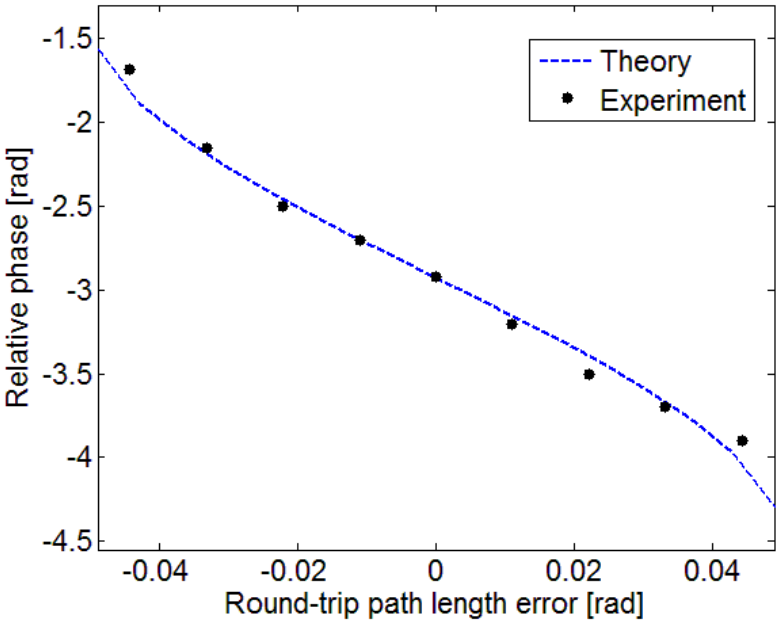

Fig .5.6 Relative phase of fundamental supermode components.

Fig. 5.7 shows the cavity power loss as a function of path length error for a second experiment where the blocking filter is adjusted to promote the in-phase mode. From these data, it is apparent that the phase error tolerance region becomes wider and the phase-error loss increases.

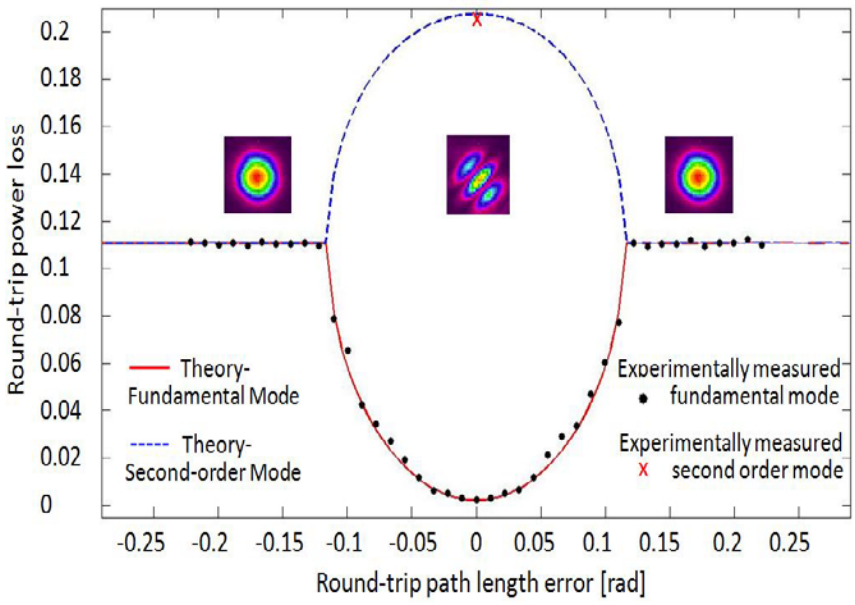

Fig. 5.7 Phase-error loss vs. path length error (in-phase fundamental supermode).

Finally, a third experiment was performed where the blocking filter was adjusted to promote the out-of-phase mode (as in the first experiment) but the thickness of the filter was changed from 2.7 μm to 5 μm. The data, shown in Fig. 5.8, indicate that a thicker filter widens the region where modal discrimination takes place at the expense of introducing more loss to both supermodes. Comparing Figs. 5.4, 5.7 and 5.8, an apparent tradeoff can be observed between mode loss and phase error tolerance.

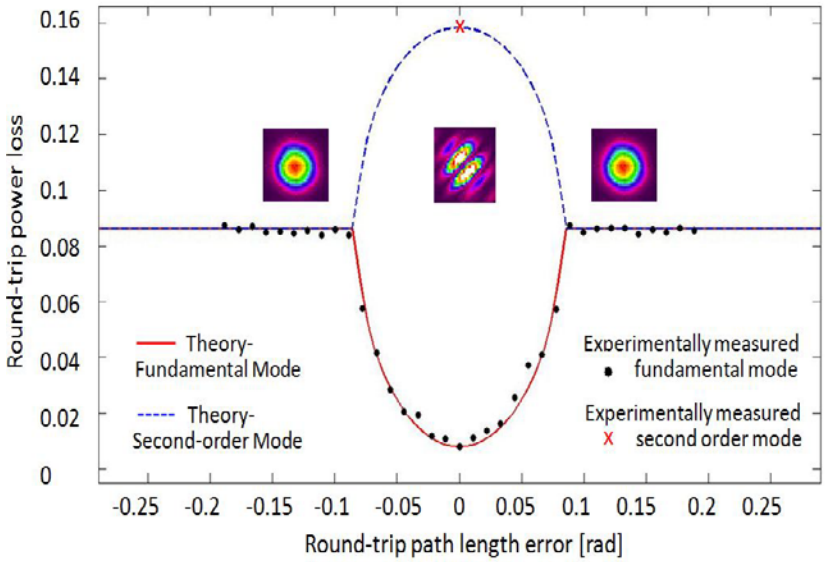

Fig. 5.8 Phase-error loss vs. path length error (thicker wire).

As predicted by Eq. 4.16, the two supermodes in the large phase error region (i.e. when Eq. 4.20 is satisfied) have the same power loss per round trip. However, their frequencies begin to separate from each other as the path length phase error increases. Since in this region the cavity supports two supermodes of slightly different frequencies, we can use the beating between the two modes to measure the frequency difference. A high-speed detector was used to measure the output light from the right side of the cavity and the beat frequency extracted by Fourier analysis. Fig. 5.9 shows the measured beat frequencies as a function of round-trip path length error, together with the predicted frequency difference from our numerical model. The data points corresponding to path length errors between 0.08 rad. and 0.16 rad. could not be measured using the beating technique. To determine the reason, we placed a quarter wave plate and a polarizer external to the left hand side of the cavity, and examined the power in a single supermode

with a high speed detector. The quarter wave plate was necessary to convert the generally elliptically polarized light from a single supermode into a linearly polarized beam, where it could be either selected or rejected by the linear polarizer. It was apparent that in this phase error region, the supermodes were alternating in a quasi-periodic manner, and there were no times when both modes were present simultaneously. Thus, no beat signal could be observed.

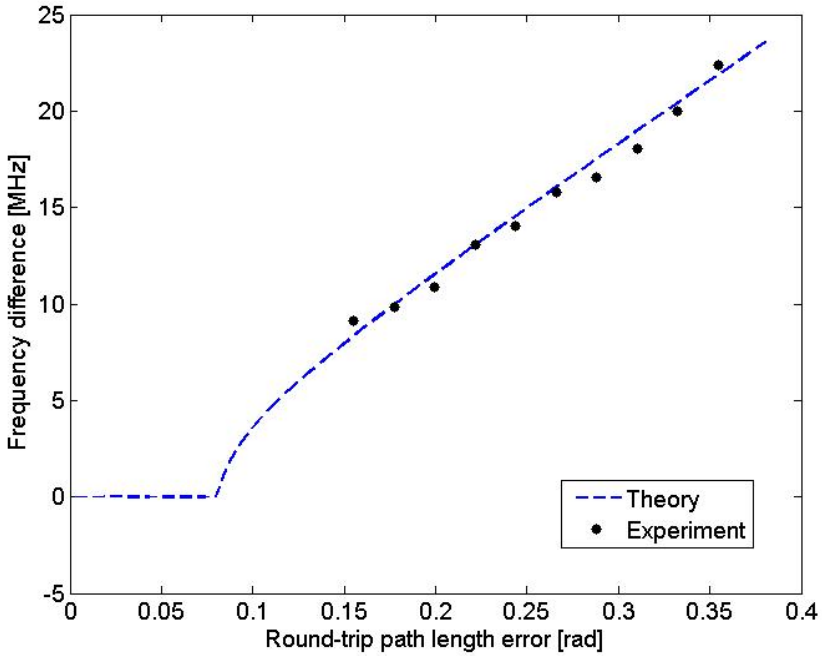

Fig. 5.9 Frequency difference between the two supermodes.

Chapter 6 Coherent Beam Shaping

The supermodes of most coherently combined cavities contain multiple lobes in the far field. Laser beam shaping, the control of the irradiance and phase profile of the output of a laser, is an enabling technology to convert the supermodes to desired shapes. For applications that need to maximize the on-axis irradiance, the desired beam shape is uniform in both amplitude and phase within the optical aperture. Focusing this flat-top mode delivers the power into the central lobe in the far field. This chapter introduces several beam evaluation parameters, including the M^2 parameter, Strehl ratio and power in the bucket in Chapter 6.1. In Chapter 6.2, a TEM01* mode is converted into a flat-top mode to concentrate the energy into an intense spot in the far field. In Chapter 6.3, the supermode of a self-Fourier cavity containing 21 lasers is converted to a quasi-flat-top shape and most power is delivered to the central far-field lobe.

6.1 Beam Quality Parameters

Three beam quality parameters are reviewed in this chapter. They are used to evaluate the beam quality of a laser beam for various applications.

6.1.1 M^2 parameter

The M^2 parameter, also called beam propagation parameter, is a common measure of the beam quality of a laser beam. The M^2 parameter is defined as the product of beam radius and the half-angle beam divergence divided by λ/π, where λ is the wavelength of the beam [26] [27]. The M^2 definition is based on the second-order moments of the intensity vs. distance and intensity vs. angle functions. A Gaussian beam is said to be diffraction-limited and has an M^2 parameter of 1. A laser beam is often compared with a Gaussian beam and is said to be "M^2 times diffraction-limited". A Hermite-Gaussian beam TEM_{mn} has an M^2 parameter of (2m+1) in the x direction and (2n+1) in the y direction. The M^2 parameter of a laser beam limits the degree to which the laser beam can be focused for a given beam divergence angle, which is limited by the numerical aperture of the focusing lens. The radiance of a laser beam is determined by the M^2 parameter together with the laser power.

6.1.2 Strehl ratio

The Strehl ratio is defined as the ratio of the on-axis far-field intensity of a beam propagated from a near-field hard aperture to that of an ideal field (uniform in amplitude and phase) filling the same hard aperture [7]. The Strehl ratio cannot be larger than 1.

The supermodes of most coherently combined cavities contain many lobes in the far field. To increase the far-field on-axis intensity, it is useful to increase the Strehl ratio of the laser beam by increasing the fill factor (the ratio of the area of the beam containing light to the total area of the mode) and shaping the amplitude and phase [28]. Chapter 6.2 and 6.3 provide two examples of increasing the Strehl ratio of laser beams by beam shaping methods.

6.1.3 Power in the bucket

The power-in-the-bucket curves plot the integrated fractional power of a laser beam within a given radius as a function of radius [26] [27]. A power-in-the-bucket curve can be obtained using circular buckets, or rectangular scans in x and y using a single knife edge and some appropriate mathematical manipulation. Plotting a power-in-the-bucket curve on a logarithmic horizontal scale gives an even more graphic indication of any pedestal effects in a laser beam by showing how far out one must go to capture, for example, 95% or 99% of the total power in a given beam.

6.2 Beam shaping of the TEM01* mode

Some lasers naturally produce higher-order modes, and conversion of these mode shapes to more useful ones is required. The TEM01* mode is common in CO_2 lasers developed for EUV lithography. The TEM01* mode (also called donut mode) has a circular intensity profile with a null at the center (Fig. 6.1). It is comprised of two orthogonal TEM01 modes. In order to form the highest intensity possible on the target, ray mapping techniques are used to convert the TEM01* mode to the flat-top mode.

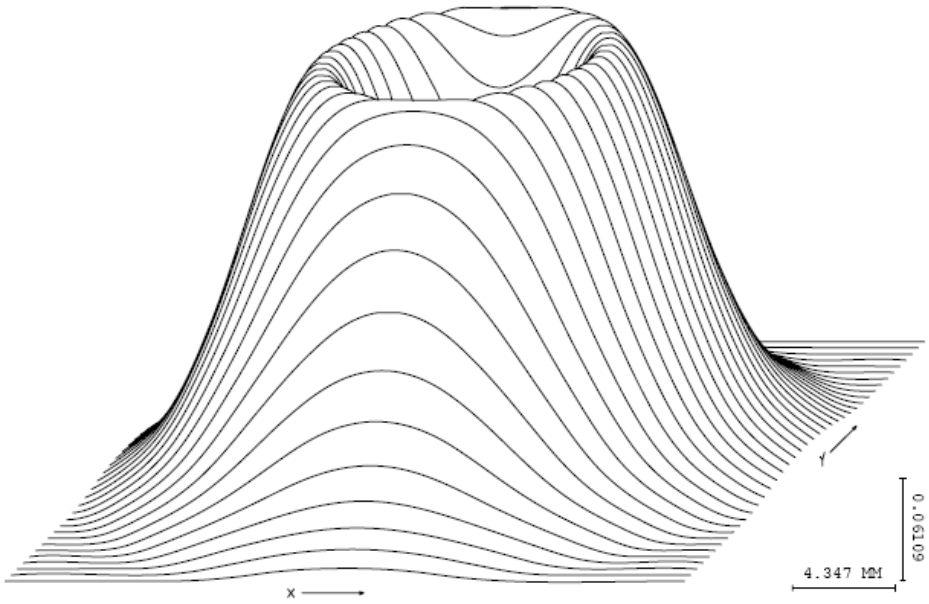

Fig.6.1 Intensity distribution of the TEM01* mode

Ray mapping involves dividing up the beam into equal energy sections and adjusting the phase tilt of the input beam to move the energy from one section to another. Once the ray mappings have been established, they form a set of slopes that can be integrated to create a desired phase profile.

6.2.1 Layout of the TEM01* mode shaping optics

The configuration of the beam shaping apparatus is shown in Fig. 6.2. The setup consists of a plano-concave lens and a plano-convex lens. The on-axis thicknesses of the two lenses are t_1 and t_2 respectively. The separation between the two lenses is d. The refractive indexes of the two lenses are both n. The coordinate of a point on the concave surface is expressed as (r, z) and the coordinate of a point on the convex surface is (R, Z) [29]. The refractive index of the medium between the two lenses is n_0.

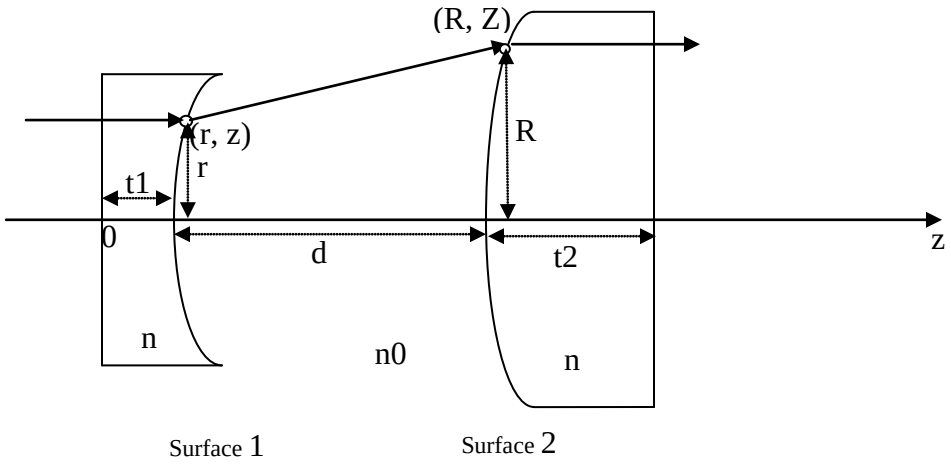

Fig.6.2 Layout of the TEM01* mode shaping optics [29]

The incoming and exiting bundles of rays are assumed to be parallel to the optical axis (z axis). The system is designed to convert the intensity profile from the donut shape to the flat-top shape. The intensity distribution of the incoming beam (TEM01* mode) is expressed as,

$$\sigma(r) = C_1 (\frac{r}{r_0})^2 e^{-2(\frac{r}{r_0})^2} \tag{6.1}$$

where C_1 is a constant. The conservation of energy relates the incoming beam (TEM01*mode) and the exiting beam (flat-top mode) by the following equation [29]:

$$\int_0^{2\pi} d\theta \int_0^r \sigma(r) r dr = \int_0^{2\pi} d\theta \int_0^R \Sigma(R) R dR \tag{6.2}$$

$\Sigma(R)$ is the energy density within a radial distance R. Since the exiting beam is an equal-power top-hat beam, $\Sigma(R)$ is a constant. The relationship of R and r can be derived from Eq. 6.2. For any pairs of r and R, the integrated fractional power within the corresponding circular regions of the incoming beam and the exiting beam is always equal. When $R = R_{\max}$ and $r = r_{\max}$ the numerical value of Σ can be calculated ($r_{\max}$ and $R_{\max}$ are the working apertures of the first and second lenses respectively).

Rays passing through the radial points (r,z) are refracted by the first lens to the radial points (R,Z). By using the eikonal equation that links wave optics and ray optics and applying the Snell's law, the following differential equation is obtained [29]:

$$[(1-(\frac{n}{n_0})^2)(Z-z)^2 - (\frac{n}{n_0})^2 (R-r)^2](z')^2 + 2(R-r)(Z-z)z' + (R-r)^2 = 0 \tag{6.3}$$

The second lens makes the exiting rays parallel to the optical axis and keeps the wavefront unchanged. Using the constant OPL (optical path length) condition, the following equation is obtained [29].

$$Z = z + \frac{n(n-n_0)d + [n_0^2(n-1)^2 d^2 + (n^2 - n_0^2)(R-r)^2]^{1/2}}{n^2 - n_0^2} \tag{6.4}$$

Thus based on Eqs. 6.2, 6.3 and 6.4, the desired phase profiles of the two lenses can be calculated.

The parameters used in the calculations are listed below:

r_{max}	R_{max}	d	n_0	n	t_1	t_2	r_0
14.4 mm	22.5 mm	150 mm	1	1.51872	10 mm	10 mm	8 mm

Table 6.1 Parameters used in the TEM01* mode shaping by two lenses

6.2.2 Plots of the desired profiles of the two lenses

The numerical data calculated from the differential equations are plotted in Fig. 6.3. These curves characterize the shape of the two surfaces. High order polynomials are used to fit these curves, and the mathematical expressions are given by Eqs. 6.5 and 6.6.

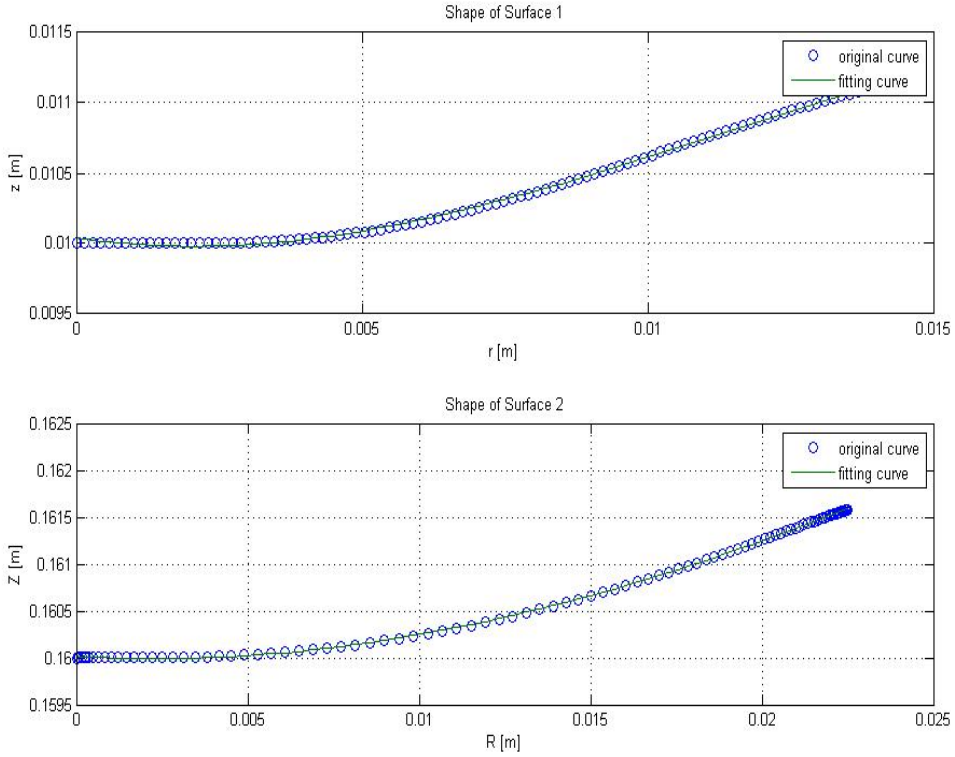

Fig.6.3 Plots of surface shapes

Surface 1: [m]

$$z(r)=-483.6691r^3+16.7499r^2-0.0622r+0.0100 \quad (6.5)$$

Surface 2: [m]

$$Z(R)=-31.9164R^3+4.7759R^2-0.0212R+0.1600 \quad (6.6)$$

6.2.3 CODEV simulation of the TEM01* mode shaping designs

CODE V is a software developed by Optical Research Associates to model, analyze, optimize, and provide fabrication support for the development of optical systems for diverse applications. We used CODE V to verify the mathematical expressions given by Eqs. 6.5 and 6.6.

Figures 6.4 shows the intensity distribution of a quasi-flat-top mode converted from the TEM01* mode. The null at the center is eliminated and the intensity distribution is quasi-uniform. The central area is not completely flat and slightly lower than the side area.

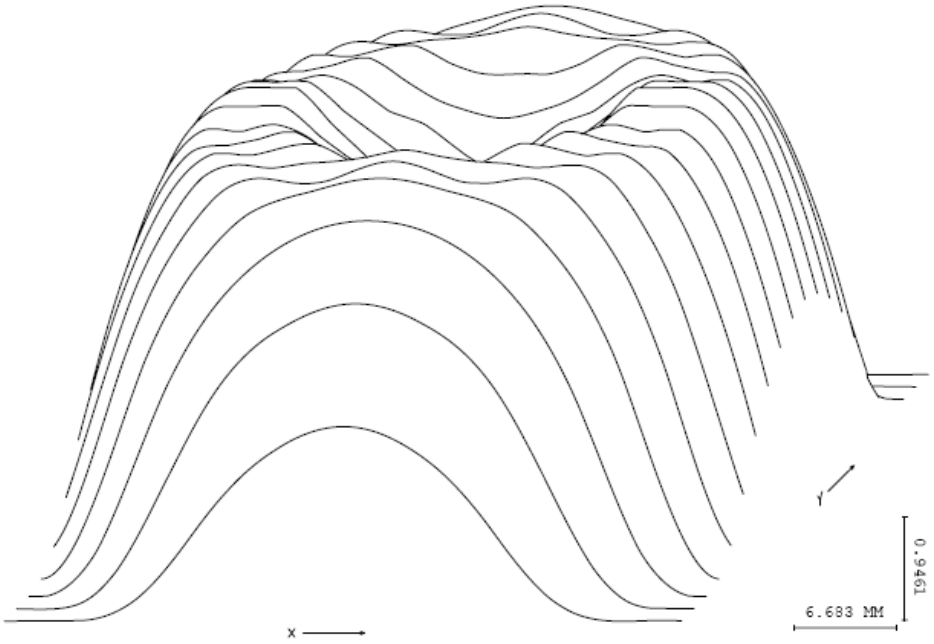

Fig.6.4 A quasi-flat-top mode converted from the TEM01* mode

6.2.4 Layout of the Cassegrain optics

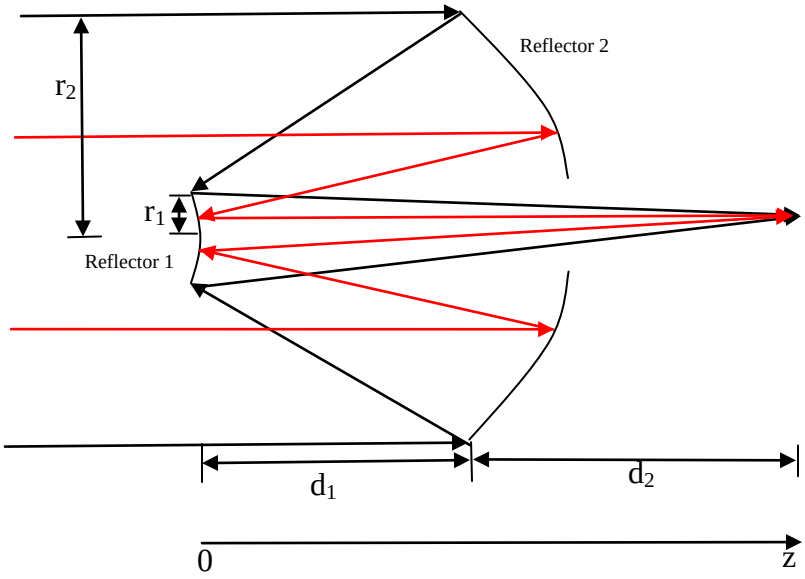

Fig.6.5 Layout of the Cassegrain optics

To increase the compactness of the beam shaping apparatus, we explore the Cassegrain reflector. The Cassegrain reflector is a combination of a primary concave mirror and a secondary convex mirror, often used in optical telescopes and radio antennas. In a symmetrical Cassegrain reflector, both mirrors are aligned about the optical axis and the primary mirror contains a hole in the center.

The setup of the Cassegrain reflector is shown in Fig. 6.5. Compared to the apparatus in Fig. 6.2, the Cassegrain reflector not only converts the beam shape, but also shrinks the beam size. The parameters used in the calculations are listed below,

r_1	r_2	d_1	d_2	r_0
1 cm	10 cm	60 cm	40 cm	5 cm

Table 6.2 Parameters used in the TEM01* mode shaping by the Cassegrain setup

The collimated incoming TEM01* mode is reflected by the primary mirror onto the secondary mirror. The ray mapping divides the beam into equal energy sections and adjusts the phase tilt of the input beam to evenly distribute the energy among all the sections. The secondary mirror focuses the beam to a single point that is one meter away. Fig. 6.6 shows the desired profiles of the two reflectors. The mathematical expressions of the fitting polynomials are given by Eqs. 6.7 and 6.8.

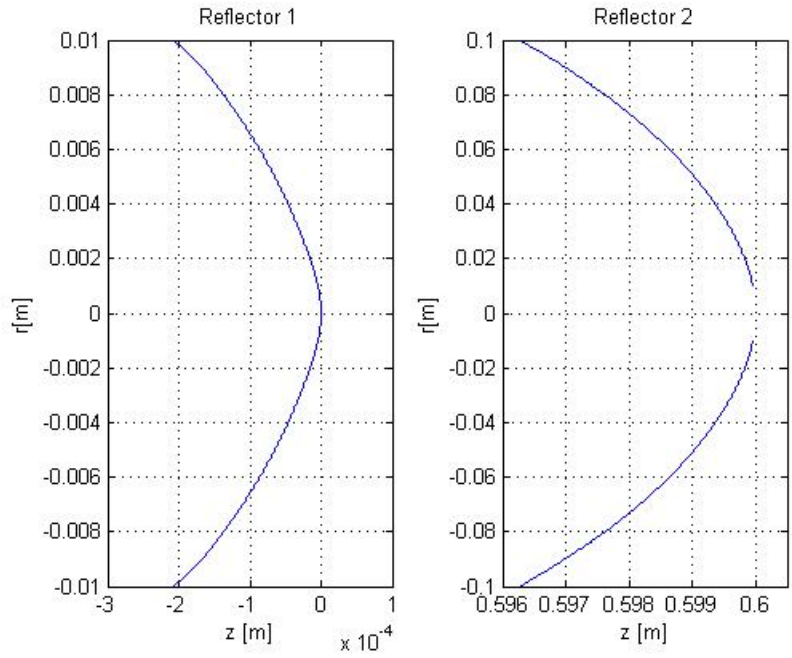

Fig.6.6 Plots of reflector shapes

Reflector 1: [m]

$$z(r)=-1.0932\times10^{11}r^{7}+2.6301\times10^{9}r^{6}-1.2104\times10^{7}r^{5}-3.4631\times10^{4}r^{4}+9.7738\times10^{2}r^{3}-5.6675r^{2} \quad (6.7)$$

Reflector 2: [m]

$$z(r)=-10.1177r^{4}+1.8437r^{3}-0.4541r^{2}-0.0001r+0.6 \quad (6.8)$$

6.2.5 Beam quality comparison

We compare the beam quality of the TEM00 mode, the TEM01* mode and the flat-top mode based on the Strehl ratio and the power-in-the-bucket curve. The light fields of the TEM00 mode, the TEM01*mode and the flat-top mode at the lens pupil are given by,

$$u_0(r) = a_0 e^{-(r/\omega_0)^2} \tag{6.9}$$

$$u_1(r) = \frac{a_1 r}{\omega_1} e^{-(r/\omega_1)^2} \tag{6.10}$$

$$u_f(r) = a_f circ(\frac{r}{R}) = \begin{cases} a_f, & r < R \\ \frac{1}{2} a_f, & \text{r=R} \\ 0, & r > R \end{cases} \tag{6.11}$$

where ω_0 is the radius of the TEM00 mode and ω_1 is the radius of the TEM01* mode. All of the three modes illuminate the same optical lens of a fixed pupil size *R*. The integrated fractional power of the three modes is normalized before comparison. We compare the far-field on-axis intensity of the three modes by performing a Fourier transform of the field distribution at the lens pupil and calculating the far-field peak intensity. We calculate the far-field on-axis intensity of the TEM00 mode and TEM01*mode for various values of ω_0 and ω_1 and the highest on-axis intensity is chosen for comparison.

	Near-field amplitude	Beam waist	Clipping amplitude	Far-field on-axis intensity
TEM00 Mode	a_0=0.446	ω_0=1.79	28.7%	0.814
TEM01* Mode	a_1=0.855	ω_1=1.32	35.6%	0.866
Flat-top Mode	a_f=0.282	R=2	100%	1

Table 6.3 Comparison of the TEM00 mode, the TEM01*mode and the flat-top mode

Table 6.3 lists the near-field amplitude, beam waist and the far-field on-axis intensity of the three modes. The Strehl ratio is increased by 14% when the TEM01* mode is converted to the flat-top mode (Fig. 6.7).

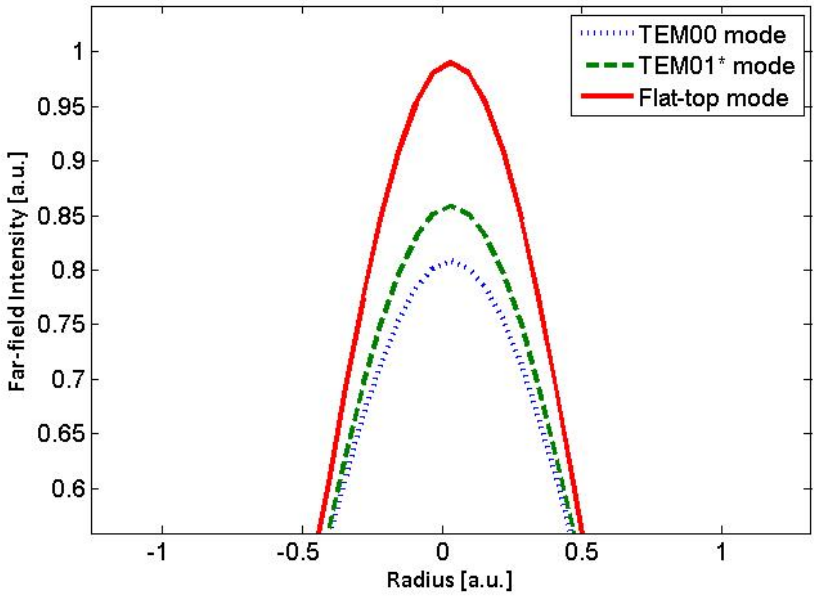

Fig. 6.7 Intensity distribution at the focused spot

Fig. 6.8 shows the power-in-the-bucket curves of the three modes. The flat-top mode curve rises faster when the radius is less than 0.12. The flat-top mode contains more power in the central area (radius<0.12) in the far field.

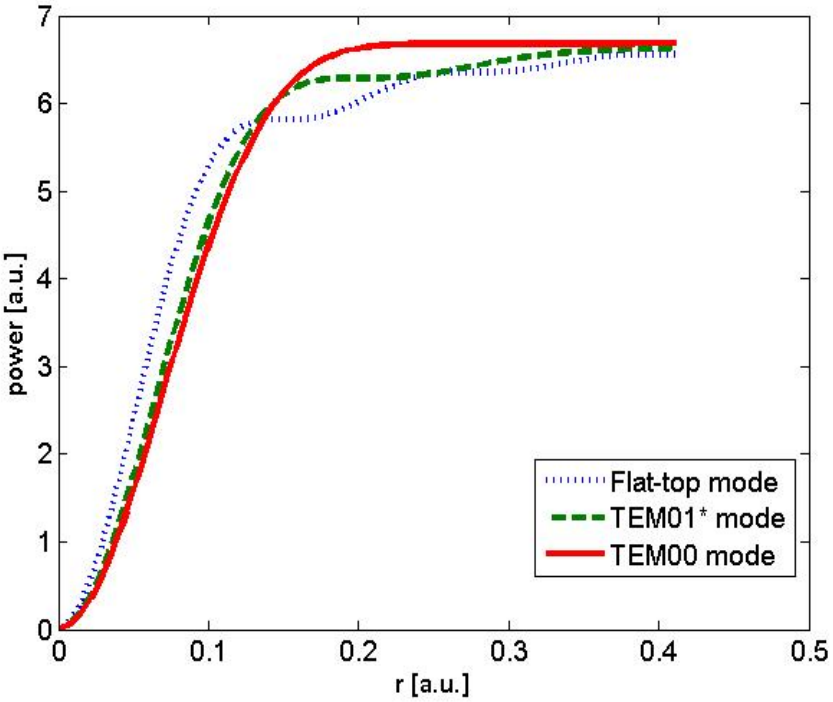

Fig.6.8 Power in the bucket curves of the three modes

6.3 Beam shaping of phase-locked laser arrays

In this section we describe several ways to convert the supermodes of phase-locked laser arrays into a quasi-flat-top mode. The conversions are based on the phase modifications in the Fourier plane.

6.3.1 Aperture filling technique

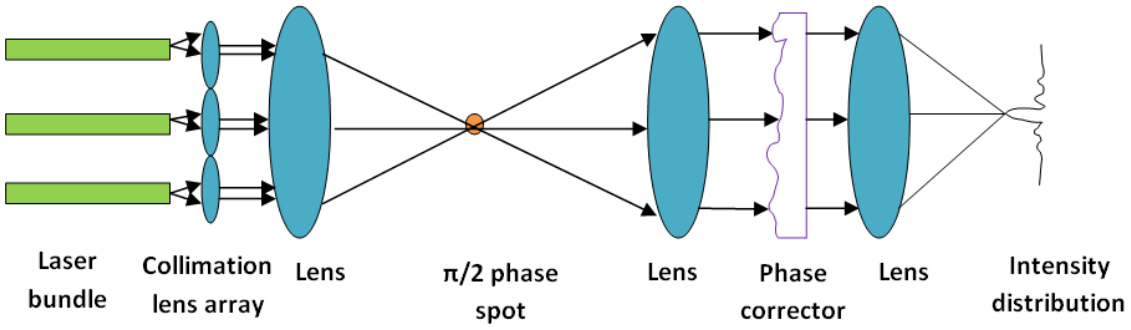

Fig. 6.9 Beam shaping apparatus using the aperture filling technique

Swanson et al. proposed an aperture filling technique based on the inverse Zernike effect that performed a transformation on the electric field emitted by a phase-locked laser array [30]. The result of this transformation was an electric field that was nearly uniform in amplitude and varied in phase. A phase-correcting plate was then employed to eliminate the resulting phase variations.

The optical setup of the aperture filling beam shaping is shown in Fig. 6.9. A $\pi/2$ phase spot is placed in the center of the Fourier plane of a 4*f* optical system. The phase spot is used to convert the non-uniformity in amplitude to a non-uniformity in phase.

Case 1: flat-top envelope (25 lasers)

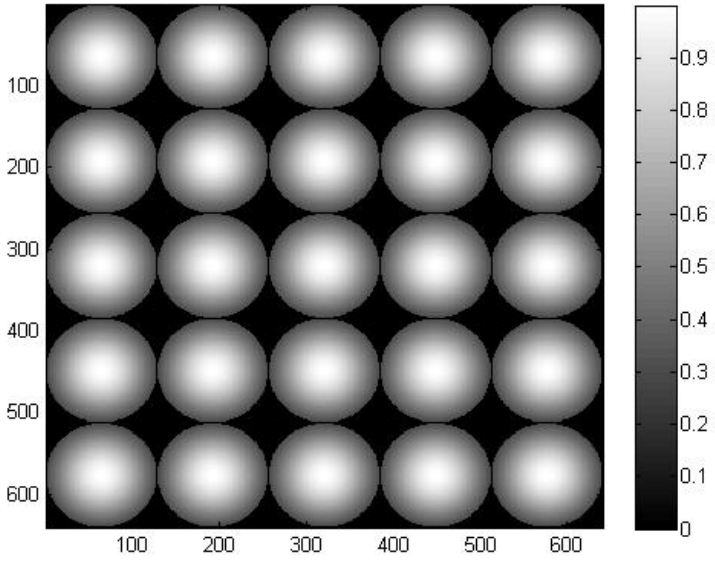

Fig. 6.10 Amplitude distribution of the laser array with a flat-top envelope.

The first input beam consists of the outputs of an array of 25 identical lasers. Each laser emits a Gaussian beam and all these Gaussians have the same beam width and amplitude. Fig. 6.10 shows the intensity distribution of the laser array. Fig. 6.11 shows the converted amplitude which has a smaller variance than the input amplitude in Fig. 6.10. Fig. 6.12 shows the cosine phase corrector that eliminates phase variations. The cosine phase corrector is not the ideal phase corrector, but is an approximation that would be easy to make.

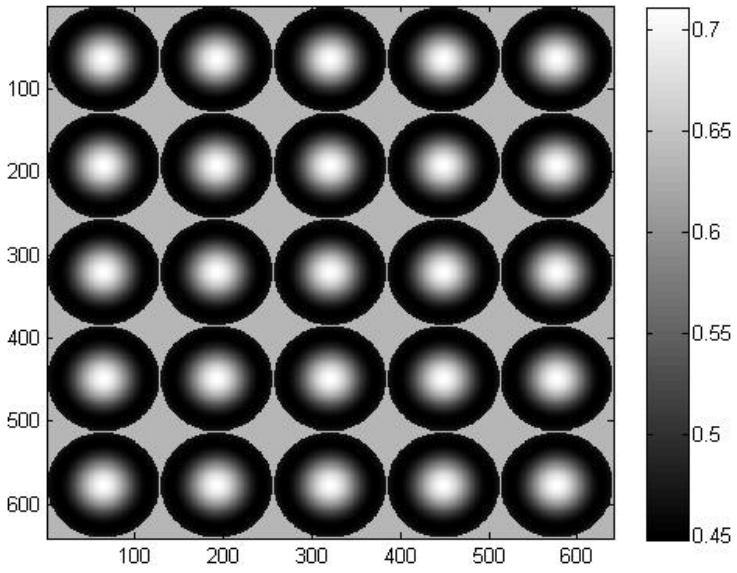

Fig. 6.11 The converted amplitude using the aperture filling technique

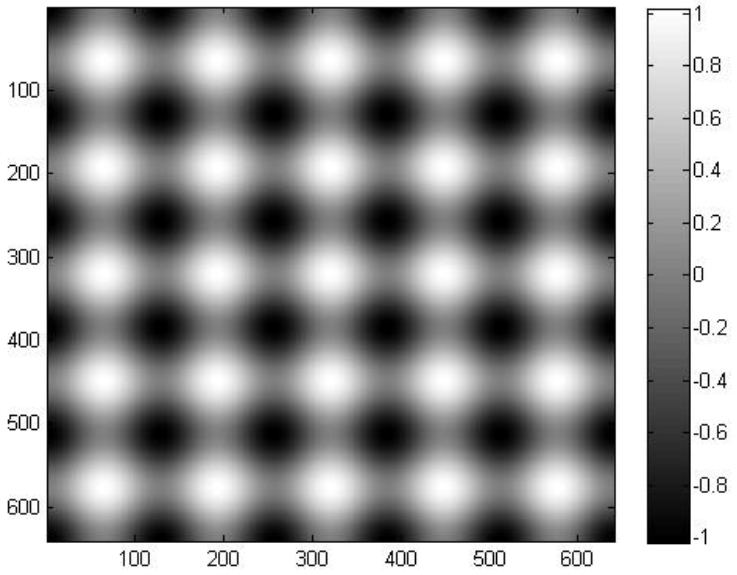

Fig. 6.12 Cosine phase corrector

Three parameters are defined to calculate the far-field power fraction in the central lobe. R1 is defined as the ratio of the power that passes through the circular apertures of the collimation lens array to the total input power. R2 is defined as the ratio of the power in the central lobe to the total power in the far field. R is defined as the product of R1 and R2. If the beam of the laser array is focused directly after the collimation lens array (without using the aperture filling technique), the maximum R is R=62.1% when R1=90.7% and R2=68.4%. The aperture filling technique improves the maximum R to 89.2% when R1=96.2% and R2=92.7%. Thus 27% more light are concentrated in the central lobe after employing the aperture filling technique. Table 6.4 lists the comparison of the far-field power fraction in the central lobe.

	R1	R2	R
w/o aperture filling	90.7%	68.4%	62.1%
w/ aperture filling	96.2%	92.7%	89.2%

Table 6.4 Comparison of the far-field power fraction in the central lobe
(25 lasers, flat envelope)

Case 2: Gaussian envelope (21 lasers)

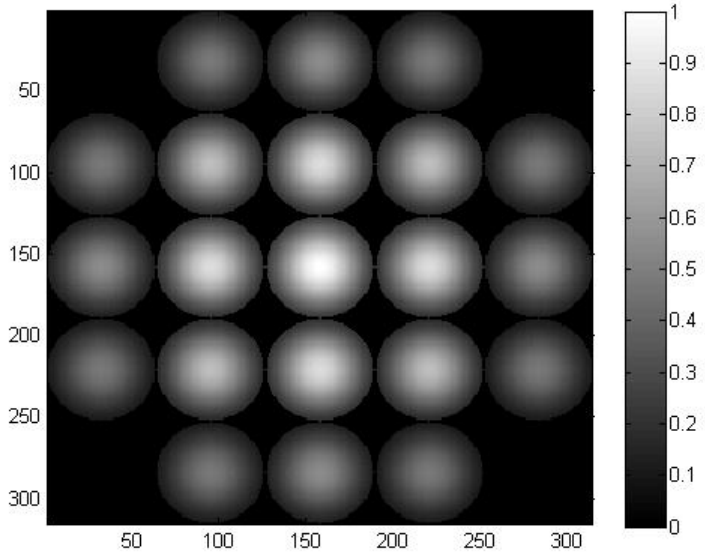

Fig. 6.13 Amplitude distribution of the laser array with a Gaussian envelope.

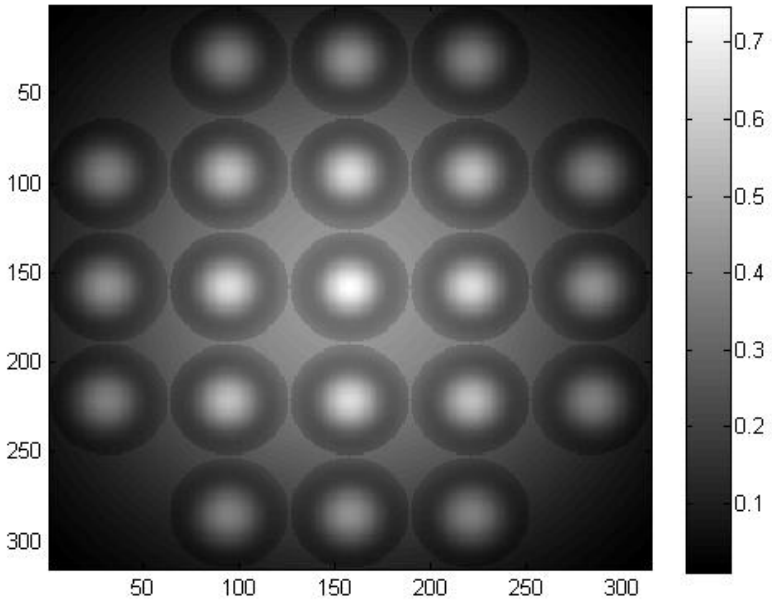

Fig. 6.14 The converted amplitude using the aperture filling technique

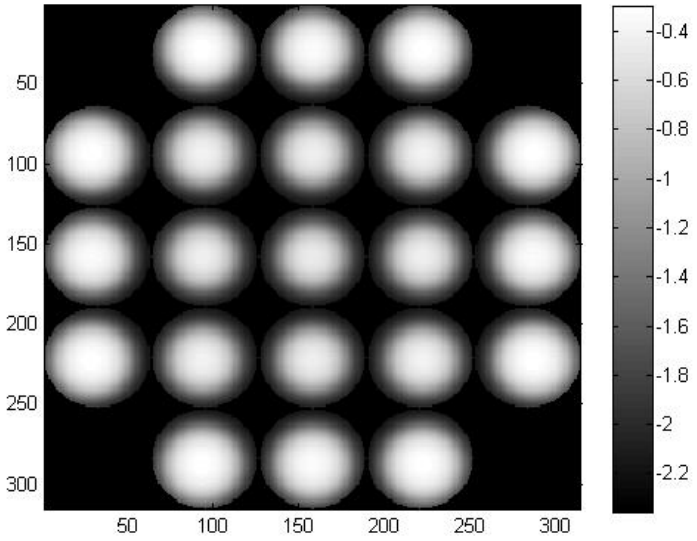

Fig. 6.15 The ideal phase corrector

The second input beam consists of the outputs of an array of 21 individual lasers. The field distribution is an array of Gaussians with an overall Gaussian envelope. This incoming beam is of particular interest because it is the fundamental mode of the self-Fourier beam combining cavity. Fig. 6.13 shows the intensity distribution of the laser array. Fig. 6.14 shows the converted amplitude which has a smaller variance than the input amplitude in Fig. 6.13. Fig. 6.15 shows the ideal phase corrector that eliminates phase variations.

If the light from the laser array is focused directly after the collimation lens array (without using the aperture filling technique), the maximum R is R=56.2% when R1=95.1% and R2=59.1%. The aperture filling technique improves the maximum R to 89.4% when R1=98.5% and R2=90.8% and an ideal phase corrector is used (Fig. 6.15). If

a binary phase corrector is used (Fig. 6.16), the maximum R is improved to 80.2% when R1= 99.2% and R2= 80.9%. Table 6.2 lists the comparison of the far-field power fraction in the central lobe. Table 6.5 lists the comparison of the far-field power fraction in the central lobe.

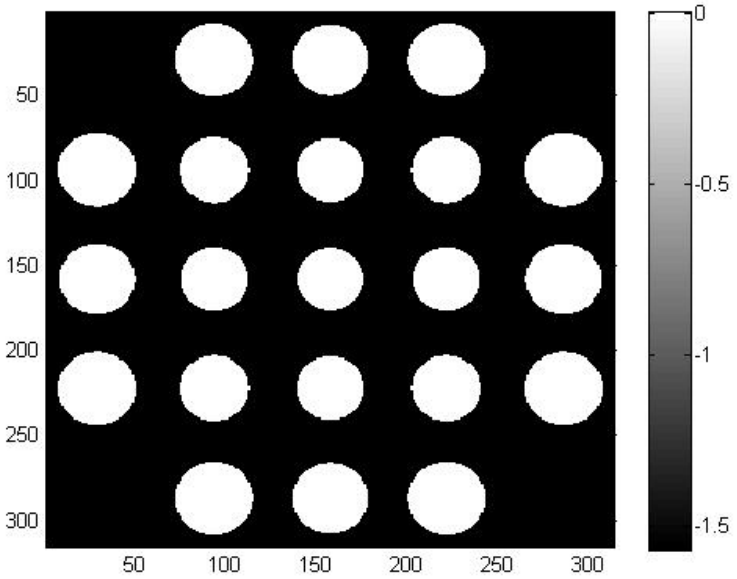

Fig. 6.16 binary phase corrector (0 or $\pi/2$)

	R1	R2	R
w/o aperture filling	95.1%	59.1%	56.2%
w/ aperture filling (ideal corrector)	98.5%	90.8%	89.4%
w/ aperture filling (binary corrector)	99.2%	80.9%	80.2%

Table 6.5 Comparison of the far-field power fraction in the central lobe (21 lasers, Gaussian envelope)

6.3.2 Beam shaping based on multi-lobe phase modifications in the Fourier plane

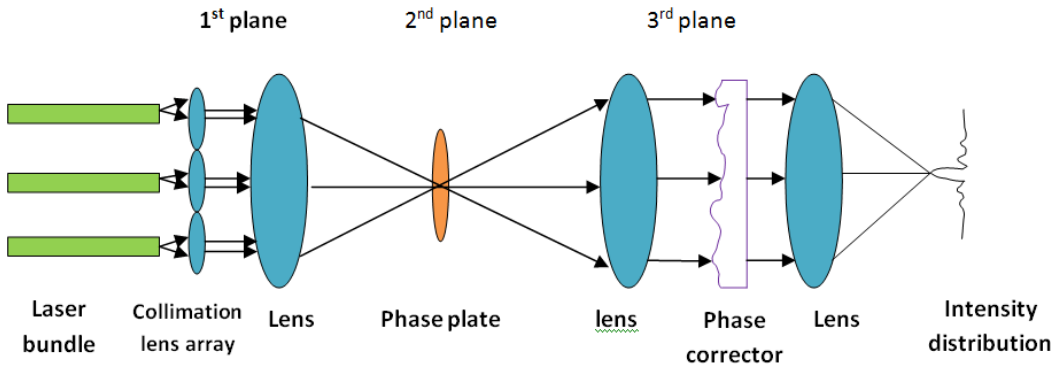

Fig. 6.17 Optical setup of the generalized amplitude-to-phase conversion method [28]

M. Khajavikhan proposed the generalized amplitude-to-phase conversion method in 2008 [28]. The previous aperture filling technique modifies only the central lobe of the laser beam in the Fourier plane. The generalized amplitude-to-phase conversion method, however, modifies all the lobes of the laser beam in the Fourier plane. This method circumvents the limitations of Swanson's method and offers high combining efficiencies for laser arrays with arbitrary fill factors.

Figure 6.17 shows the configuration of the generalized amplitude-to-phase conversion apparatus. In the Fourier plane, a phase plate replaces the phase spot to modify all the lobes. The optimum phase plate pattern is obtained by performing Fourier transform iteration between the 2nd plane and the 3rd plane. The iteration is based on the Gerchberg-Saxton phase retrieving algorithm (Fig. 6.18). The Gerchberg-Saxton algorithm was originally invented in connection with the problem of reconstructing phase from two

intensity measurements. The algorithm involves iterative Fourier transformation back and forth between the object and Fourier domains and application of the measured data or known constraints in each domain. In our case the amplitudes in the second and third plane are constraints and the phases are variables. The iteration is performed until a uniform amplitude is obtained in the third plane.

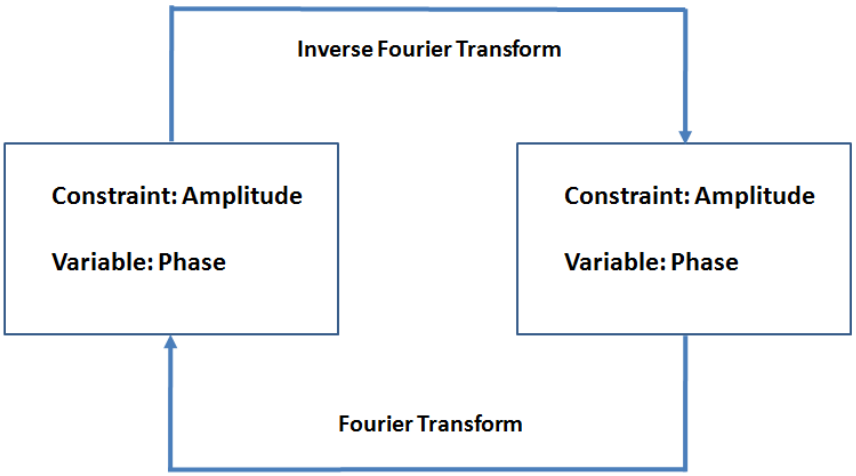

Fig. 6.18 Gerchberg-Saxton algorithm [31]

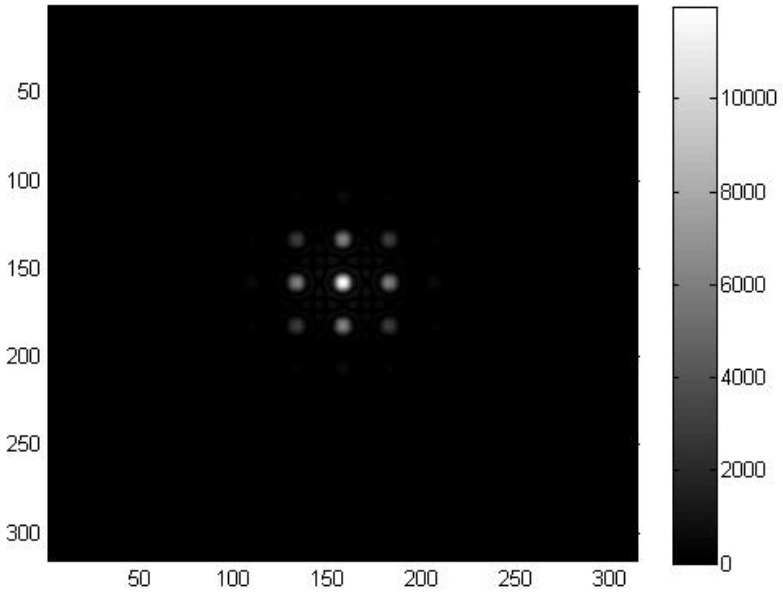

Fig. 6.19 Amplitude in the 2nd plane.

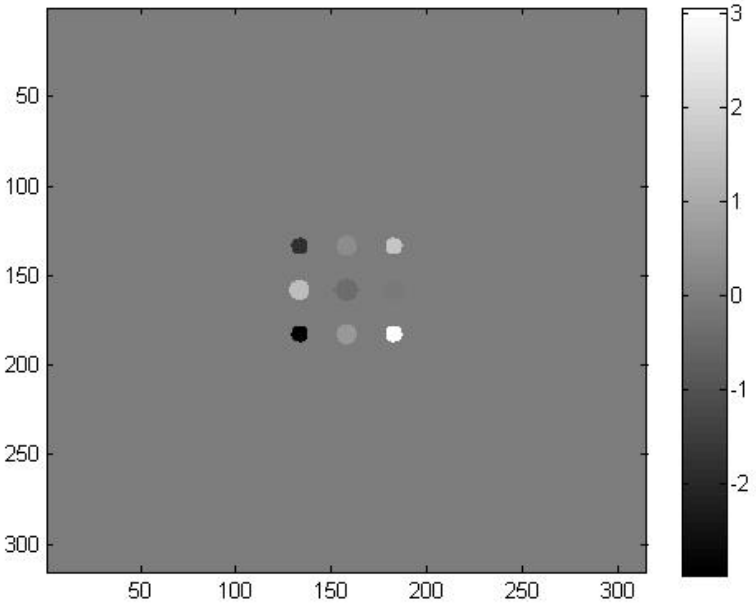

Fig. 6.20 phase plate in the 2nd plane.

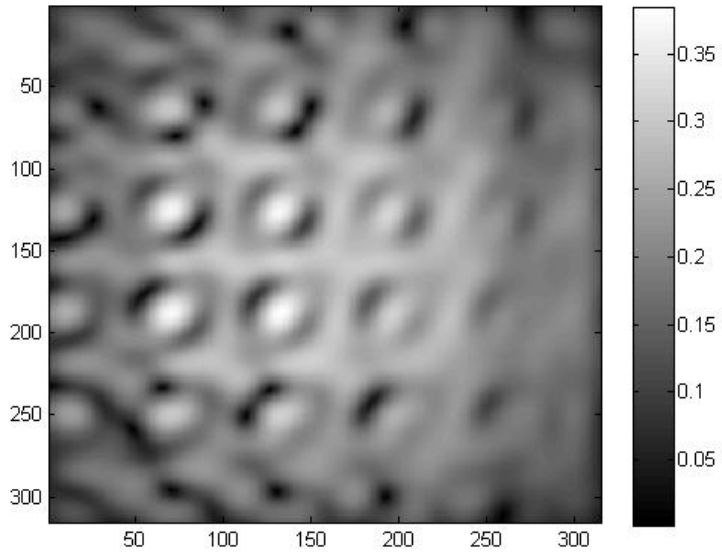

Fig. 6.21 Amplitude in the 3rd plane

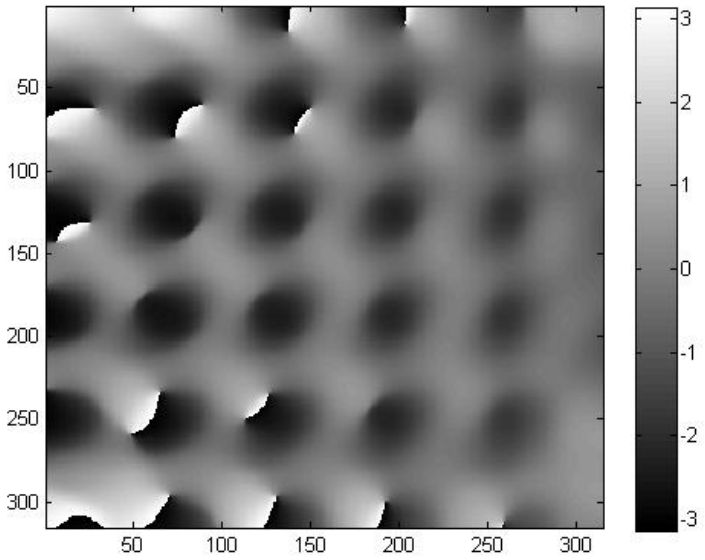

Fig. 6.22 phase corrector in the 3 rd plane

Fig. 6.19 and 6.20 are the amplitude and phase distributions in the 2nd plane. Figure 6.21 and 6.22 are the amplitude and phase distributions in the 3rd plane. Table 6.6 shows the comparison of the far-field power fraction in the central lobe. The generalized amplitude-

to-phase conversion method improves the far-field power fraction in the central lobe from 56% to 94%.

Gaussian envelope	R1	R2	R
w/o any technique	95.1%	59.1%	56.2%
w/ aperture filling (ideal corrector)	98.5%	90.8%	89.4%
w/ aperture filling (binary corrector)	99.2%	80.9%	80.2%
w/ generalized amplitude-to-phase conversion method	99.9%	94.4%	94.4%

Table 6.6 Comparison of the far-field power fraction in the central lobe (generalized amplitude-to-phase conversion method)

Chapter 7 Conclusion

The cold cavity analysis is performed to explain the modal properties of several coherent beam combining cavities. The supermodes of a two-laser spatially filtered cavity are found to exhibit two distinctly different types of behavior depending on the phase error. When the error is small, the two modes present different cavity loss values and can be differentiated by gain. However, cavities containing path length errors greater than a critical value produce modes with identical losses and different resonant frequencies. Laser systems with more than two channels can be modeled by similar methods and exhibit somewhat more complex behavior.

A diode-pumped Nd:YAG laser cavity is built to verify the above path length sensitivity theory. The measured results support the modal theory to within experimental error. The behavior of this coherently coupled system is distinctly different from those based on beamsplitters and Dammann gratings. We find a narrow range of path length errors where the supermodes can be discriminated by gain. Outside this range, it is not possible to discriminate between the two modes and incoherent lasing results.

The multi-lobe far-field distributions of phased-locked laser arrays are unsuitable for many laser applications. Beam shaping techniques are used to convert the supermodes of laser arrays into a flat-top mode that is uniform in amplitude and phase. The flat-top mode is useful in applications which require power concentration in the far field. Both

the aperture filling technique and the generalized amplitude-to-phase conversion method convert the amplitude non-uniformity to phase non-uniformity. After subsequently eliminating the phase variations, both amplitude and phase become quasi-uniform. The aperture filling technique modifies only the central lobe in the Fourier plane whereas the generalized amplitude-to-phase conversion method imposes phase modifications in the entire Fourier plane. The generalized amplitude-to-phase conversion method offers higher combining efficiencies for laser arrays with arbitrary fill factors, but at the expense of increasing the complexity of the phase plate in the Fourier plane.

References

[1] T. H. Maiman, "Stimulated Optical Radiation in Ruby," Nature, 187 4736, pp. 493-494 (1960)

[2] W. Koechner, "Thermal Lensing in a Nd:YAG Laser Rod," Appl. Opt. 9, 2548-2553 (1970)

[3] R.G. Smith, "Optical Power Handling Capacity of Low Loss Optical Fibers as Determined by Stimulated Raman and Brillouin Scattering," Appl. Opt. 11, 2489-2494 (1972)

[4] R.W. Boyd, Nonlinear Optics, Boston: Academic Press, Inc., 1992

[5] B. Chann, R. K. Huang, L.J. Missaggia, C. T. Harris, Z. L. Liau, A. K. Goyal, J. P. Donnelly, T. Y. Fan, A. Sanchez-Rubio, and G. W. Turner, "Near-diffraction-limited diode laser arrays by wavelength beam combining," Opt. Lett. 30, 2104-2106 (2005)

[6] V. Daneu, A. Sanchez, T. Y. Fan, H. K. Choi, G. W. Turner, and C. C. Cook, "Spectral beam combining of a broad-stripe diode laser array in an external cavity," Opt. Lett. 25, 405-407 (2000)

[7] T.Y. Fan, “Laser beam combining for high-power, high-radiance sources,” IEEE J. Sel. Topics Quantum Electron., vol. 11, no. 3, pp. 567–577, May/Jun. 2005.

[8] David J. Brady, "Multiplex sensors and the constant radiance theorem," Opt. Lett. 27, 16-18 (2002)

[9] Y. Jeong, J. Sahu, D. Payne, and J. Nilsson, "Ytterbium-doped large-core fiber laser with 1.36 kW continuous-wave output power," Opt. Express 12, 6088-6092 (2004)

[10] E. Kapon, J. Katz, and A. Yariv, “Supermode analysis of phase-locked arrays of semiconductor lasers,” Opt. Lett., vol. 9, pp. 125–127, 1984.

[11] W. Marshall and J. Katz, “Direct analysis of gain-guided phase-locked semiconductor laser arrays,” IEEE J. Quantum Electron., vol. QE-22, no. 6, pp. 827–832, Jun. 1986.

[12] M. Khajavikhan, and J. R. Leger, "Modal Analysis of Path Length Sensitivity in Superposition Architectures for Coherent Laser Beam Combining," JSTQE, vol.15, pp.281-290, 2009.

[13] J. R. Leger, G. J. Swanson, andW. B. Veldkamp, “Coherent laser addition using binary phase gratings,” Appl. Opt., vol. 26, pp. 4391–4399, 1987.

[14] A. A. Golubentsev, V. V. Likhanskii, and A. P. Napartovich, “Theory of phase locking of an array of lasers,” Sov. Phys. JETP, vol. 66, pp. 676–682, 1987.

[15] J. R. Leger, “Lateral mode control of an AlGaAs laser array in a Talbot cavity,” Appl. Phys. Lett., vol. 55, pp. 334–336, 1989.

[16] C. J. Corcoran and K. Pasch, “Modal analysis of a self-Fourier laser cavity,” J. Opt. A: Pure Appl. Opt., vol. 7, pp. L1–L7, 2005.

[17] C J Corcoran and K A Pasch, “Self-Fourier functions and coherent laser combination”, J. Phys. A: Math. Gen. 37 L461 (2004)

[18] C. J. Corcoran and F. Durville, “Experimental demonstration of a phase locked laser array using a self-Fourier cavity,” Appl. Phys. Lett., vol. 86, pp. 201118-1–201118-3, 2005.

[19] E. Philipp-Rutz, “Spatially coherent beam formation and mode locking of an array of solid-state lasers,” IEEE J. Quantum Electron., vol. QE-14, no. 2, pp. 112–118, Feb. 1978.

[20] R. H. Rediker, R. P. Schloss, and L. J. Van Ruyven, “Operation of individual diode lasers as a coherent ensemble controlled by a spatial filter within an external cavity,” Appl. Phys. Lett., vol. 46, pp. 133–135, Oct. 1985.

[21] D. Mehuys, W. Streifer, R. G. Waarts, and D. F. Welch, “Modal analysis of linear Talbot-cavity semiconductor lasers,” Opt. Lett., vol. 16, pp. 823–825, 1991.

[22] C. Wan, B. Tiffany, and J. Leger, "Analysis of Path Length Sensitivity in Coherent Beam Combining by Spatial Filtering," IEEE J. Quantum Electron., vol. 47, no. 6, pp. 770-776, June, 2011

[23] Siegman, Lasers, University Science Books, 1986, pp. 585,781.

[24] C. Wan, J. Leger, "Experimental Measurements of Path Length Sensitivity in Coherent Beam Combining by Spatial Filtering," Quantum Electronics, IEEE Journal of , vol.48, no.8, pp.1045-1051, Aug. 2012

[25] M. Khajavikhan, K. John, and J. R. Leger, " Experimental Measurements of Supermodes in Superposition Architectures for Coherent Laser Beam Combining," IEEE J. Quantum Electron., vol. 46, no. 8, pp. 1221–1231, Aug. 2010.

[26] A. E. Siegman, "Defining, measuring, and optimizing laser beam quality", Proc. SPIE 1868, 2 (1993)

[27] A. E. Siegman, "How to (Maybe) Measure Laser Beam Quality," in DPSS (Diode Pumped Solid State) Lasers: Applications and Issues, M. Dowley, ed., Vol. 17 of OSA Trends in Optics and Photonics (Optical Society of America, 1998), paper MQ1.

[28] M. Khajavikhan, A. Hoyer-Leitzel, and J. R. Leger, "Efficient conversion of light from sparse laser arrays into single-lobed far field using phase structures," Opt. Lett. 33, 2377-2379 (2008)

[29] F. Dickey and S. Holswade, Laser Beam Shaping:Theory and Techniques, CRC Press 2000 Pg 163-213

[30] G. J. Swanson, J. R. Leger, and M. Holz, "Aperture filling of phase-locked laser arrays," Opt. Lett. 12, 245-247 (1987)

[31] J. Fienup, "Phase retrieval algorithms: a comparison," APPLIED OPTICS, Vol. 21, No. 15 (1982)